

1 **Revealing Hidden Oxygen Variability in the North Pacific: A Two-**  
2 **Decade Analysis Using GOBAI-O<sub>2</sub>**

3  
4

5 Miho Ishizu<sup>1,2</sup>, Tomomichi Ogata<sup>3</sup>

6

7 *<sup>1</sup>Center for Climate Physics, Institute for Basic Science, Busan 46241, Republic of Korea*

8 *<sup>2</sup>Pusan National University, Tonghapgigyegwan Bldg 2 Busandaehak-ro, 63 beon-gil, Geumjeong-gu,*  
9 *Busan 46241, Republic of Korea*

10 *<sup>3</sup>Japan Agency for Marine-Earth Science and Technology, Environmental Variability Prediction and*  
11 *Application Research Group, Yokohama Institute for Earth Sciences, 3173-25 Showa-machi,*  
12 *Kanagawa-ku, Yokohama 236-0001, Japan*

13 To whom correspondence should be addressed: Miho Ishizu (mishizu@pusan.ac.kr)

14

15

16 **Abstract**

17 Oceanic dissolved oxygen concentrations are thought to be declining under ongoing global warming,  
18 yet their variability remains less well understood than that of physical parameters such as temperature  
19 and salinity, primarily due to the limited spatial and temporal coverage of oxygen observation. Here,  
20 we examine linear trends in potential temperature, salinity, and dissolved oxygen in the North Pacific  
21 over the past two decades ( 2004–2023 ), using the GOBAI-O<sub>2</sub>-v2.2 dataset (Version 4.4). We compare  
22 the diagnosed oxygen trends with those of physical parameters to reveal the spatial structure of recent  
23 changes. The oxygen trends inferred from GOBAI-O<sub>2</sub> are broadly consistent with trends observed  
24 along ship-based hydrographic repeat lines. While basin-scale deoxygenation is evident, we also  
25 identify localized oxygen increases on specific density surfaces. By relating these patterns to the

26 surrounding physical environment, we find that the spatial heterogeneity in oxygen trends is consistent  
27 with known oceanographic processes, including the southward retreat of the oxygen minimum layer  
28 and the northward migration of a front separating the subtropical and subarctic gyres. These results  
29 underscore the value of GOBAI-O<sub>2</sub> data in linking physical variability to previously unrecognized  
30 biological and biogeochemical patterns in the ocean.

31

32

### 33 **Plain Language Summary**

34 1. We investigated how potential temperature, salinity, and dissolved oxygen have changed in the  
35 North Pacific over the past 20 years using the GOBAI-O<sub>2</sub>-v2.2 dataset (Version 4.4), and we  
36 examined the physical processes responsible for these trends.

37 2. The trends identified in this study are broadly consistent with findings from previous research, and  
38 improved spatial coverage of the GOBAI-O<sub>2</sub> allowed us to reveal connections between regional  
39 patterns that we previously only partially understood.

40 3. Overall, dissolved oxygen decreased across much of the North Pacific. However, some regions  
41 showed increasing oxygen levels, indicating that the changes were not uniform. These non-uniform  
42 patterns reflect known physical ocean processes. For example, higher oxygen levels in the northern  
43 North Pacific are consistent with a northward shift of the front separating the subtropical and  
44 subarctic gyres. In the equatorial Pacific, the reduced westward extent of the oxygen minimum  
45 layer corresponds to a weakening and poleward shift of the North Equatorial Countercurrent  
46 ( NECC ) on interdecadal timescales.

47 4. These findings provide new evidence that links large-scale physical ocean changes to previously  
48 unclear changes in biological and biogeochemical observations.

49

50 Keywords: dissolved oxygen, 20-year linear trends, Bio-Argo float data, global warming

51

## 52 **1. Introduction**

53 Over recent decades, the global ocean has experienced a decline in its dissolved oxygen inventory, a  
54 trend projected to continue through the 21st century [ Keeling et al., 2010; Breitburg et al., 2018;  
55 Stramma and Schmidtko, 2021; Limburg et al., 2020; Ito et al., 2017, 2024; Kolodziejczyk et al., 2024 ].  
56 This deoxygenation is driven in part by reduced ocean oxygen solubility under rising sea-surface  
57 temperatures, which promotes oxygen outgassing. In addition, enhanced stratification and a slowdown  
58 of ocean circulation under global warming can reduce interior ventilation and oxygen supply [ Keeling  
59 et al., 2010; Bopp et al. 2013; Ito et al. 2017 ]. Ocean oxygen loss can negatively affect aerobic marine  
60 organisms [ Pörtner and Farrell, 2008; Sampaio et al., 2021 ], alter biogeochemical cycles, and  
61 potentially induce climate-relevant feedback [ Berman-Frank et al., 2008 ]. Historical deoxygenation  
62 has been inferred from globally distributed observations [ Helm et al., 2011; Schmidtko et al., 2017;  
63 Ito et al., 2017; Takatani et al., 2012; Sasano et al., 2015; Lauvset et al., 2022b ], and Earth system  
64 models have been used to simulate both historical and future changes in ocean oxygen [ Bopp et al.,  
65 2013; Kwiatkowski et al., 2020; Li et al. 2020 ].

66

67 Observed oxygen trends have traditionally been assessed using the discrete measurements of dissolved  
68 oxygen concentration (  $O_2$  ), typically obtained by Winkler titration [ Winkler, 1988 ]. These  
69 measurements are also used to calibrate electrode- and, more recently, optode-based oxygen sensors  
70 mounted on conductivity-temperature-depth ( CTD ) profilers [ Helm et al. 2011; Schmidtko et al.,  
71 2017; Lauvset et al., 2022b ]. Although programs such as WOCE, CLIVAR, and GO-SHIP have  
72 collected high-quality oxygen measurements globally, repeat occupation intervals are commonly on  
73 the order of a decade, limiting the ability to robustly quantify annual to seasonal variability. Higher-

74 frequency ship-based observations exist in a few regions [ Takatani et al. 2012; Sasano et al., 2015 ],  
75 but their spatial coverage is limited. Consequently, despite attempts to characterize basin-scale patterns  
76 [ Ito et al. 2017; Stramma et al. 2020; Kolodziejczyk et al. 2024 ], observational constraints have  
77 hampered a spatially and temporally comprehensive understanding of dissolved oxygen variability and  
78 trends.

79

80 Oxygen sensors were first deployed on Argo profiling floats in the mid-2000s. Since then,  
81 approximately 1,800 oxygen-equipped floats have been deployed worldwide, substantially advancing  
82 the observational basis for assessing oxygen variability and trends [ Sharp et al., 2023 ]. The expansion  
83 toward a global biogeochemical ( BGC ) Argo network has improved sampling in regions that were  
84 previously sparsely observed [ Claustre et al., 2020 ]. In parallel, major progress has been made in  
85 calibration, adjustments, and quality control of oxygen measurements, including pre-deployment drift  
86 corrections [ D'Asaro and McNeil, 2013; Johnson et al., 2015; Bittig and Körtzinger, 2015; Bushinsky  
87 et al., 2016; Drucker and Riser, 2016; Nicholson and Feen, 2017 ], climatology-based calibrations  
88 [ Takeshita et al., 2013 ], in-air oxygen measurement calibrations [ Körtzinger et al., 2005; Bittig and  
89 Körtzinger, 2015; Johnson et al., 2015; Bushinsky et al., 2016 ], post-deployment drift corrections  
90 [ Johnson et al., 2017; Bittig et al., 2018a, b ], and the standardized delayed-mode quality control  
91 procedures [ Maurer et al., 2021 ]. Together, these developments have reduced uncertainty and  
92 improved the consistency of optode-based [ O<sub>2</sub> ] measurements from Argo floats.

93

94 To date, oxygen observations from Argo floats have been used primarily in regional process studies,  
95 including air-sea oxygen exchange [ Wolf et al., 2018 ], upper-ocean primary production [ Alkire et al.,  
96 2012; Estapa et al., 2019 ], biological pump efficiency [ Johnson and Bif, 2021 ], and the dynamics of  
97 the oxygen minimum zone [ Udaya Bhaskar et al., 2021 ]. Recently, Sharp et al. [ 2023 ] produced a

98 four-dimensional gridded [ O<sub>2</sub> ] product, GOBAI-O<sub>2</sub> ( Gridded Ocean Biogeochemistry from Artificial  
99 Intelligence ( AI ) – Oxygen ). GOBAI-O<sub>2</sub> is constructed using machine-learning methods trained on  
100 oxygen observations and designed to reconstruct spatial patterns, seasonal cycles, and decadal  
101 variability, particularly in regions where observational data gaps coincide with high background O<sub>2</sub>  
102 variability.

103

104 In the North Pacific, several studies have documented heterogeneous oxygen trends. Using an  
105 objectively mapped monthly climatology of O<sub>2</sub> based on the World Ocean Database 2013 ( WOD13 )  
106 [ Boyer et al. 2013 ], Ito et al. [ 2017 ] reported multidecadal variability and trends in dissolved O<sub>2</sub> in  
107 the surface-layer oxygen from 1958 to 2013. Sasano et al. [ 2015 ], using the high-frequency shipboard  
108 sections along the 137°E and 165°E lines from 1987 to 2011, reported oxygen declines in the northern  
109 subtropical to subtropical-subarctic transition zones of  $-0.45 \pm 0.16 \mu\text{mol/kg/yr}$  at 25.3  $\sigma_{\theta}$  and  $-0.45 \pm$   
110  $0.14 \mu\text{mol/kg/yr}$  at 26.8  $\sigma_{\theta}$ , respectively. They also identified a significant oxygen increase in the  
111 tropical Oxygen Minimum Layer (OML) of  $+0.36 \pm 0.004 \mu\text{mol/kg/yr}$ , highlighting pronounced spatial  
112 heterogeneity in oxygen trends. At broader scales, Stramma et al. [ 2020 ] analyzed historical bottle  
113 data and reported links between oxygen variability and climate modes such as the Pacific Decadal  
114 Oscillation ( PDO ) and the North Pacific Gyre Oscillation (NPGO), although sparse sampling makes  
115 it difficult to robustly connect regional trends to physical mechanisms. Collectively, previous studies  
116 indicate that oxygen changes in the North Pacific can be strong, spatially non-uniform, and potentially  
117 driven by both circulation/ventilation changes and biologically mediated oxygen consumption  
118 [ Sasano et al. 2015; 2018; Ito et al. 2017; 2024; Stramma et al., 2020; Kolodziejczyk et al. 2024 ].

119

120

121 Because observational opportunities to quantify trends in dissolved oxygen—together with concomitant  
122 changes in temperature and salinity—remain limited, gridded products such as GOBAI-O<sub>2</sub> are

123 becoming increasingly valuable for basin-scale analyses. In this study, we use GOBAI-O<sub>2</sub> to quantify  
124 linear trends in potential temperature, salinity, and dissolved oxygen in the North Pacific over 2004–  
125 2023 and examine how their trends are connected in both depth and density space. We further discuss  
126 the extent to which the diagnosed oxygen trends can be interpreted in terms of physical drivers,  
127 including surface warming, stratification changes, and circulation variability in the North Pacific.

128

## 129 **2. Data and Methods**

### 130 **2.1 GOBAI-O<sub>2</sub> dataset**

131 We use GOBAI-O<sub>2</sub>-v2.2 (Version 4.4), a four-dimensional, monthly gridded product of dissolved  
132 oxygen ( O<sub>2</sub> ) in the ocean interior, generated using machine learning ( ML ) algorithms trained on both  
133 Argo float oxygen measurements and ship-based discrete observations [ Sharp et al., 2023 ]. GOBAI-  
134 O<sub>2</sub> is mapped onto the temperature-salinity fields provided by the global Argo array [ Roemmich and  
135 Gilson, 2009 ]. The underlying oxygen training database combines ship-based measurements from  
136 GLODAPv2.2022 and Argo float data distributed through the Argo Global Data Assembly Centers,  
137 after quality control [ Sharp et al., 2023 ] ( <https://doi.org/10.25921/z72m-yz67> ).

138

139 According to Sharp et al. [ 2023 ], the float data used in GOBAI-O<sub>2</sub> were filtered to retain only delayed-  
140 mode adjusted profiles with quality flags of 1 (good), 2 (probably good), or 8  
141 (interpolated/extrapolated) for pressure, temperature, salinity, and dissolved oxygen. Among all  
142 available float profiles, 51.4% underwent quality control through comparison with climatological  
143 fields from the World Ocean Atlas (WOA) or the Commonwealth Scientific and Industrial Research  
144 Organisation Regional Sea Atlas (CARS). An additional 30.3% were evaluated using atmospheric  
145 oxygen concentration measurements, and 7.0% were quality controlled through comparison with in-  
146 water measurements (WOD, OMS assuming an oxygen zero, or deployment-time CTD profiles). A

147 further 5.3% were adjusted using in-situ optode calibration based on the method of Drucker and Riser  
148 [2016], 3.3% were adjusted by other methods, 1.9% were unclassified, and the remaining 0.9% were  
149 not adjusted.

150

151 The ML models predict O<sub>2</sub> using predictors that include absolute salinity, conservative temperature,  
152 potential density anomaly, hydrostatic pressure, bottom depth, and additional spatiotemporal  
153 covariates representing geographic, seasonal, and interannual variability. Biological processes are not  
154 explicitly parameterized in the ML framework; however spatiotemporal covariates can implicitly  
155 capture biological influences to some extent [ Giglio et al., 2018 ].

156

157 GOBAI-O<sub>2</sub> is produced using two ML approaches: feed-forward networks (FNNs) and random forest  
158 regression ( RFRs, [ Breiman, 2001 ] ). The final O<sub>2</sub> estimate at each grid point is taken as the mean  
159 of the FNN and RFR predictions. The dataset spans 2004–2023 at monthly resolution on a 1° × 1°  
160 latitude –longitude grid, covering 86% of the global ocean area. The product is provided on 58 vertical  
161 levels from the surface to ~2,000 m. Sharp et al. [ 2023 ] reported 0.79 ± 0.04% per decade decrease  
162 in the oxygen inventory of the upper 2000 m over 2004–2022. Full details of their data sources,  
163 processing, algorithm training, evaluation, and uncertainty estimation are given in Sharp et al. [ 2023 ].

164

## 165 **2.2 Uncertainty estimates**

166 GOBAI-O<sub>2</sub> provides an uncertainty estimate for each gridded O<sub>2</sub> value, constructed by combining  
167 independent uncertainty components in quadrature [ Sharp et al., 2023 ]:

$$168 \quad u([O_2])_{tot.} = \sqrt{u([O_2])_{meas.}^2 + u([O_2])_{grid.}^2 + u([O_2])_{alg.}^2} \quad (1),$$

169 where  $u([O_2])_{meas.}^2$  represents measurement uncertainty of the underlying observations,

170  $u([O_2])_{grid}^2$  ) is the gridding uncertainty associated with representing a four-dimensional  
171 spatiotemporal volume by a single value, and  $u([O_2])_{alg}^2$  is the algorithmic uncertainty arising from  
172 the ML estimation. We use  $u([O_2])_{tot}$  to characterize uncertainty in  $O_2$  and to propagate uncertainty  
173 into our oxygen trend estimates (Figs. 1–4). In most figures, we incorporate the mean uncertainty when  
174 estimating linear  $O_2$  trends.

175

### 176 **2.3 Vertical grid and interpolation for isopycnal analysis**

177 GOBAI- $O_2$  is provided on a  $1^\circ \times 1^\circ$  horizontal grid with 58 depth levels: 2.5, 10, 30, 40, 50, 60, 70,  
178 80, 90, 100, 110, 120, 130, 140, 150, 160, 170, 182.5, 200, 220, 240, 260, 280, 300, 320, 340, 360,  
179 380, 400, 420, 440, 462.5, 500, 550, 600, 650, 700, 750, 800, 850, 900, 950, 1000, 1050, 1100, 1150,  
180 1200, 1250, 1300, 1350, 1412.5, 1500, 1600, 1700, 1800, 1900 and 1975 m. The enhanced near-surface  
181 vertical resolution is important for resolving strong gradients in temperature, salinity, density, and  
182 oxygen within the mixed layer [ Kara et al., 2000 ].

183

184 For analysis performed in density space, we interpolate the original depth-level data to 1-m vertical  
185 grid using cubic spline interpolation and then evaluate linear trends on a  $1^\circ \times 1^\circ \times 1$  m grid. This  
186 approach enables computation of trends as a function of latitude (  $1^\circ$  bins ) and potential density  
187 anomaly (  $0.1\sigma_\theta$  bins ) ( Figs. 4–7 ). To evaluate sensitivity to interpolation choices, we repeated the  
188 analysis using linear, shape-preserving cubic ( PCHIP ) interpolation and using coarser vertical grids  
189 ( 2 m and 5 m ). The resulting trend patterns show no material differences among interpolation methods  
190 ( Figs. S1 ( a, b ) and S2 ( a, b ) ). The 5-m grid cannot resolve densities lighter than  $24.0\sigma_\theta$  at some  
191 latitudes; however, the main features are preserved across all tested resolutions.

192

### 193 **2.4 OFES model output**

194 In Section 3.3.2, we additionally use output from the eddy-resolving OGCM for the Earth Simulator  
195 ( OFES ) [ Masumoto et al., 2004; 2010; Sasaki et al., 2008 ] to examine the physical context of the  
196 diagnosed variability. OFES is based on the MOM3 [ Pacanowski and Griffies, 2000 ] and uses a quasi-  
197 global domain spanning 75° S– 75°N with 0.1° x 0.1° horizontal resolution and 54 vertical levels. The  
198 model was initialized from rest using the World Ocean Atlas 1998 (WOA98) [ Boyer and Levitus,  
199 1997 ], and spun up for 50 years using climatological forcing derived from NCEP-NCAR reanalysis  
200 [ Kalnay et al., 1996 ]. After spin-up, a hindcast experiment was conducted from 1950 to 2024 using  
201 daily NCEP-NCAR forcing. Here we analyze OFES output over 1950–2023.

202

## 203 **2.5 GODAS model output**

204 In Section 3.3.2, we also use temperature and salinity fields from the NCEP Global Ocean Data  
205 Assimilation System ( GODAS ) to complement our analysis. GODAS is a global ocean reanalysis  
206 system developed at the National Centers for Environmental Prediction ( NCEP ) and is based on the  
207 Modular Ocean Model version 3 [ Pacanowski and Griffes, 2000 ]. The system assimilates surface  
208 temperature profiles, XBT data, moored buoy observations, and other in situ measurements using a  
209 three-dimensional variational ( 3DVAR ) assimilation scheme [ Behringer and Xue, 2004; Behringer,  
210 2007 ]. The GODAS reanalysis is provided on a 1° x 1° horizontal grid with enhanced meridional  
211 resolution (1/3°) near the equator and includes 40 vertical levels. The reanalysis spans from 1980 to  
212 the present and is widely used for climate diagnostics and ocean variability studies. In this study, we  
213 analyze GODAS density fields over the period 2003-2024 by using temperature and salinity.

214

## 215 **3. Results**

### 216 **3.1 Horizontal distributions of linear trends**

217 Figure 1 illustrates the horizontal and vertical distributions of linear trends in potential temperature,

218 salinity, and dissolved oxygen (  $O_2$  ), over 2004–2023. Positive trends in potential temperature are  
219 primarily confined to the surface layer above 200 m depth ( Fig. 1a–c ), with larger magnitudes at  
220 higher latitudes. In contrast, negative trends emerge below the surface in the eastern tropical area  
221 (  $180^\circ$ – $120^\circ$ W,  $5^\circ$ – $15^\circ$ N ) ( Fig. 1b ), extending westward and deepening with increasing depth ( Fig.  
222 1d–f ). Below  $\sim$ 400 m, the spatial distributions of positive and negative temperature trends differ  
223 between the subarctic and subtropical gyres.

224

225 Salinity trends exhibit generally negative values throughout the surface layer ( Fig. 1h–i ), consistent  
226 with freshening. Localized positive salinity trends are detected in the Kuroshio–Oyashio transition  
227 area and the northwest Pacific (  $140^\circ$ – $180^\circ$ E,  $20^\circ$ – $50^\circ$ N ), as well as in the tropical region (  $120^\circ$ –  
228  $170^\circ$ E,  $0^\circ$ – $10^\circ$ N ). Additional positive trends are observed along the eastern boundary off California  
229 (  $130^\circ$ – $199^\circ$ W,  $20^\circ$ – $40^\circ$ N ). Below 200 m depth, salinity trends are weaker and broadly mirror the  
230 temperature ( Fig. 1j–k ). Notably, negative salinity trends are evident around the Alaska gyre (  $170^\circ$ –  
231  $130^\circ$ W,  $40^\circ$ – $55^\circ$ N ) ( Fig. 1j–l ), a pattern that differs from the corresponding temperature trends.

232

233 Negative trends in dissolved  $O_2$  are widespread across the North Pacific and extend throughout much  
234 of the water column ( Fig. 1o–u ). Large negative trends are concentrated at higher latitudes near the  
235 surface, with their locations shifting systematically with depth. Particularly strong  $O_2$  declines are  
236 observed along the northeastern boundary (  $140^\circ$ – $130^\circ$ W,  $40^\circ$ – $50^\circ$ N ) and within the southern  
237 subtropical region (  $10^\circ$ – $25^\circ$ N ) on density surfaces between 25.2 and  $26.8\sigma_\theta$ , corresponding to depths  
238 of approximately 200–600 m ( Fig. 1q–s ). In contrast, weak positive  $O_2$  trends are detected below 200  
239 m depth in the Kuroshio–Oyashio transition zone (  $130^\circ$ – $150^\circ$ E,  $30^\circ$ – $40^\circ$ N ), extending into deeper  
240 layers and spreading northeastward across the basin ( Fig. 1r–u ).

241

242 Positive  $O_2$  trends are restricted to specific regions and depths: the tropical region at  $\sim 100$  m depth  
243 ( Fig. 1p ); the Alaska Gyre at 200–400 m depth ( Fig. 1q–r ); the western tropical region at 400–600  
244 m depth ( Fig. 1r–s ); and the Kuroshio–Oyashio transition region at similar depths ( Fig. 1r–s ). When  
245 examined as a function of latitude, the magnitudes of negative  $O_2$  trends do not depend monotonically  
246 on latitude alone. While surface-layer declines are strongest at high latitudes, the largest negative  
247 trends at intermediate depths ( 400–600 m ) occur in the mid-latitude band (  $30^\circ$ – $40^\circ$ N ). This depth-  
248 dependent latitudinal structure implies the importance of remote transports and the circulation-driven  
249 redistribution of oxygen, rather than purely local surface forcing. The underlying mechanisms are  
250 discussed further in Section 3.3.

251

252 The total uncertainty in dissolved  $O_2$ ,  $u([O_2])_{tot.}$ , exhibits pronounced regional structure ( Fig. 2a–  
253 g ). Uncertainty is largest in the North Pacific north of  $50^\circ$ N and decreases toward lower latitudes.  
254 Relatively high uncertainty values are also evident in the surface layer, and within regions of strong  
255 density gradients in the eastern tropical Pacific [ $150^\circ$ – $120^\circ$ W,  $10^\circ$ – $30^\circ$ N] at depths of 100–200 m ( Fig.  
256 2b–c ). In general, uncertainty peaks near 100 m depth and decreases with increasing depth ( Fig. 2  
257 and Figure A14 in Sharp et al. [ 2023 ] ). As shown by Sharp et al. [ 2023 ], regional variations in  
258 uncertainty are dominated by algorithmic uncertainty rather than measurement or gridding components  
259 ( Eq. 1 ). Elevated algorithmic uncertainty in the northern Pacific above  $50^\circ$ N and along the western  
260 and eastern tropical margins below  $20^\circ$ N reflects sparse observational coverage in these regions  
261 ( Figure 1 in Sharp et al. 2023 ).

262

263 To assess whether regional trends exceed the dataset uncertainty, we computed the spatial distribution  
264 of Robustness (  $R$  ), defined as  $R = |\text{trend over two decades}| / \text{uncertainty}$  ( Fig. 1v–bb ). (Note: This  
265 diagnostic provides a heuristic measure of the relative strength of the trend compared to the local

266 uncertainty, rather than a formal quantification of uncertainty propagation.) The results indicate that R  
267 exceeds or approaches high values in the eastern and western tropical zones, the Kuroshio Extension  
268 region, portions of the subpolar North Pacific, and along the 27.2–27.4  $\sigma_\theta$  density surfaces at 800–  
269 1000 m depth. Based on this metric, larger oxygen trend magnitudes correspond to higher R values,  
270 more clearly distinguishable from the background uncertainty. Thus, in the upper ocean ( 2.5–100 m ),  
271 trends are relatively robust in terms of the R metric, mainly in the northern North Pacific. At 200–400  
272 m, robust signals appear both in the northern North Pacific and along the 25.2–26.0  $\sigma_\theta$  surfaces in the  
273 southern subtropical region, as well as in the eastern and western tropics. At 600–1000 m, the trends  
274 are robust within the subtropical gyre bounded by the 27.0  $\sigma_\theta$  surface.

275

276 Compared with the previously reported historical horizontal distributions of dissolved O<sub>2</sub> reported by  
277 Ito et al. [ 2017 ] ( Figure 3 in Ito et al. 2017 ), our analysis shows a broader spatial extent of negative  
278 trends across the North Pacific. Whereas data gaps increase with depth in Ito et al. [ 2017 ], the GOBAI-  
279 O<sub>2</sub> product provides more spatially continuous coverage, yielding distributions that are consistent with  
280 surrounding regions. In addition, positive O<sub>2</sub> trends detected here in the Kuroshio–Oyashio transition  
281 zone and the northeastern North Pacific on density surfaces of 26.8–27.0 $\sigma_\theta$  ( Fig. 1r ) were not clearly  
282 evident in the earlier O<sub>2</sub> anomaly analysis. Similarly, the positive trends identified in the western  
283 tropical Pacific below 400 m depth ( Fig. 1r–t ) are stronger and more spatially coherent than those  
284 reported previously.

285

286 The positive O<sub>2</sub> trends coincide with regions of relatively low uncertainty values ( Fig. 1p–s and 1w–  
287 z ), suggesting that they represent relatively robust features that are better constrained by the high  
288 observation density of Argo profiling floats. Other regions exhibiting positive signals—the

289 northeastern North Pacific with a density range of  $26.8\text{--}27.0\sigma_\theta$  (  $170^\circ\text{E}\text{--}150^\circ\text{W}$ ,  $45\text{--}55^\circ\text{N}$ , Fig. 1r )  
290 and the tropical western Pacific (  $130^\circ\text{--}170^\circ\text{E}$ ,  $0^\circ\text{--}10^\circ\text{N}$ , Fig. 1r-t )—also correspond to areas of low  
291 uncertainty ( Fig. 1y-aa ). Consequently, these signals may reflect possible regional reoxygenation  
292 superimposed on the basin-scale deoxygenation trend.

293

294 Some localized expansions of the trend patterns, particularly in the tropical eastern Pacific ( e.g.  $170^\circ\text{--}$   
295  $130^\circ\text{W}$ ,  $0^\circ\text{--}20^\circ\text{N}$  ) may partly reflect regions of elevated uncertainty, occasionally exceeding  $15$   
296  $\mu\text{mol/kg}$  ( Fig. 1q-s; Fig. 4i ). Such large uncertainties would likely arise from sparse observations and  
297 high background variability [ Sharp et al. 2023 ]. Additional bias may stem from sensor calibration  
298 limitations in Argo oxygen measurements, especially in oxycline regions where finite optode response  
299 times can introduce systematic errors [ Bittig et al., 2014; 2018a,b ]. Despite these caveats, the spatial  
300 patterns of the diagnosed  $\text{O}_2$  trends are generally smooth and coherent across the basin. Based on  
301 statistical significance testing, most trends are significant throughout the water column ( Fig. 1o-u ).  
302 Overall, despite the uncertainties associated with the various factors discussed above, the GOBAI- $\text{O}_2$   
303 dataset provides an improved framework for diagnosing basin-scale oxygen variability and its physical  
304 drivers.

305

### 306 **3.2 Vertical sections and isopycnal density analysis of linear trends in $137^\circ\text{E}$ and $165^\circ\text{E}$ lines**

307 To facilitate direct comparison with historical ship-based observations, we examine vertical sections  
308 and isopycnal distributions of linear trends in potential temperature, salinity, and dissolved  $\text{O}_2$  along  
309 the  $137^\circ\text{E}$  and  $165^\circ\text{E}$  meridional sections ( Fig. 3 ). Ogata and Nonaka [ 2020 ] analyzed salinity data  
310 from 20 years of shipboard observations along the  $137^\circ\text{E}$  line between 1997 and 2016, while Sasano  
311 et al. [ 2015 ] analyzed temperature, salinity, and dissolved  $\text{O}_2$  data from 25 years of cruises along the

312 165°E line between 1987 and 2011.

313

314 Along both sections, large negative trends in potential temperature and salinity are concentrated along  
315 the 25.0–26.0 $\sigma_\theta$  isopycnal surfaces, corresponding to potential temperatures of approximately 10–  
316 12°C and salinities of 34.4–34.5 ( Fig. 3a, b, e, f ). In contrast, the strongest negative trends in dissolved  
317 O<sub>2</sub> occur primarily along denser isopycnals between 26.0 and 27.0 $\sigma_\theta$  ( Fig. 3c, g ). This vertical  
318 separation indicates that the regions of pronounced oxygen decline are not co-located with those of  
319 temperature and salinity trends, implying distinct controlling mechanisms.

320

321 In addition to widespread oxygen declines, pronounced positive O<sub>2</sub> trends are detected south of ~15°N  
322 below 200 m depth along the 137°E line ( Fig. 3c ). These positive trends are located near the upper  
323 boundary of the oxygen minimum layer ( OML ). Comparison with the corresponding uncertainty  
324 distributions ( Fig. 3d, h ) shows that regions exhibiting positive or negative oxygen trends generally  
325 do not coincide with areas of elevated uncertainty, indicating that these signals are robust within the  
326 GOBAI-O<sub>2</sub> framework.

327

328 The distributions of linear trends on isopycnal surfaces further highlight differences among  
329 temperatures, salinity, and dissolved O<sub>2</sub> ( Fig. 4 ). Trends in temperature and salinity are closely aligned,  
330 with warming accompanied by salinification and cooling accompanied by freshening ( Fig. 4a–b, d–  
331 e ). In the tropical region ( 5°S–5°N ), distinct positive trends in both variables are evident over the  
332 density range of 22.0–26.0 $\sigma_\theta$ . In contrast, little systematic trend is detected in the salinity minimum  
333 region ( S = 34–34.1 ) within the density range of 26.5–27.0 $\sigma_\theta$ . At higher latitudes ( 40°–50°N ), strong  
334 positive trends in both temperature and salinity are observed along the 26.0–27.0 $\sigma_\theta$  surfaces ( Fig. 4e ).

335

336 Dissolved oxygen trends exhibit a markedly different structure. Although negative  $O_2$  trends dominate  
337 overall, weak but coherent positive trends appear across the density range  $23.0\text{--}26.0\sigma_\theta$  in low-latitude  
338 regions (  $5^\circ\text{S}\text{--}5^\circ\text{N}$  ). More pronounced positive  $O_2$  trends are detected in the deeper density range of  
339  $26.0\text{--}27.0\sigma_\theta$  between  $5^\circ$  and  $10^\circ\text{N}$ . Additional weak positive trends are observed between  $10^\circ$  and  
340  $20^\circ\text{N}$  within the density range of  $23.0\text{--}25.0\sigma_\theta$  along both the  $137^\circ\text{E}$  and  $165^\circ\text{E}$  sections.

341

342 Compared with previous studies, the GOBAI- $O_2$ -based trends reveal both similarities and notable  
343 differences. The general characteristics of temperature and salinity trends are broadly consistent with  
344 those reported by Sasano et al. [ 2015 ], although the present results are spatially smoother, particularly  
345 for dissolved oxygen. This smoothness likely reflects the gridded nature of the dataset and the spatial  
346 regularization inherent in the machine-learning reconstruction. Along the  $137^\circ\text{E}$  section, the GOBAI-  
347  $O_2$  temperature and salinity fields exhibit a wider area of negative salinity trends within the density  
348 range  $22.0\text{--}24.0\sigma_\theta$  than those reported by Ogata and Nonaka [ 2020 ] using OFES output.

349

350 Ship-based observations by Sasano et al. [ 2015 ] identified patchy positive trends in oxygen within  
351 the density range  $24.5\text{--}27.5\sigma_\theta$  in the regions (  $5^\circ\text{--}15^\circ\text{N}$  and  $6^\circ\text{S}\text{--}1^\circ\text{N}$  ), as well as localized positive  
352 trends at greater depths. In contrast, the GOBAI- $O_2$  data reveal a broader, smoother, and more spatially  
353 coherent pattern of positive  $O_2$  trend spanning  $6^\circ\text{S}$  to  $5^\circ\text{N}$ . At the same time, the present analysis more  
354 clearly delineates the core regions of negative oxygen trends between  $5^\circ$  and  $15^\circ\text{N}$  along the lower  
355 isopycnals ( Fig. 3c and f ), which are characteristic of the subtropical gyre. These differences  
356 underscore the complementary nature of ship-based observations and gridded reconstructions and  
357 highlight the advantage of GOBAI- $O_2$  for resolving basin-scale and isopycnal-scale oxygen variability.

358

359 **3.3 Horizontal distribution of linear trends along isopycnal surfaces**

### 360 3.3.1 Potential temperature and salinity

361 The horizontal distributions of linear trends in potential temperature, salinity, and dissolved oxygen on  
362 specific isopycnal surfaces at 25.0, 26.0, and 26.8 $\sigma_\theta$  ( Fig. 5 ) are illustrated to examine how these  
363 trends occur and how they are connected. These density surfaces correspond to the shallower density  
364 range of Subtropical Mode Water ( STMW ), the shallower densities of Central Mode Water ( CMW )  
365 [ Suga et al., 1997; 2004 ], and the representative density of North Pacific Intermediate Water ( NPIW )  
366 [ Nakamura et al., 2000a, b; Nakamura and Awaji, 2003; Yasuda, 2004 ], respectively. STMW is  
367 formed south of the Kuroshio Extension between 30–35°N and 130–170°E, and reaches depths of  
368 approximately 400 m in late winter. It then spreads toward the subtropical front through advection  
369 across the Kuroshio recirculation area. CMW is formed in the transition area of the central North  
370 Pacific and spreads eastward along the North Pacific Current before turning southward and westward  
371 in the subtropical gyre [ Suga et al., 1997; 2004 ]. In contrast, NPIW does not outcrop during its  
372 formation process. Its origin lies in Okhotsk Sea Mode Water, which forms through overturning driven  
373 by diapycnal upwelling and tidal mixing around the Kuril Islands [ Nakamura et al., 2000a, b;  
374 Nakamura and Awaji, 2003; You, 2003; Yasuda, 2004 ] as well as double diffusions in the North Pacific  
375 [ You, 2003 ].

376

377 The linear trends on the 25.0, 26.0, and 26.8 $\sigma_\theta$  surfaces show that positive and negative tendencies  
378 appear in characteristic locations and are generally aligned with the geostrophic streamlines ( Fig. 5a–  
379 b, d–e, g–h ). Although exceptions exist, such as weak positive trends ( 150–175°E, 20–30°N ) ( Fig.  
380 5a–b ), negative trends in potential temperature and salinity dominate in the western and central North  
381 Pacific on the 25.0 and 26.0 $\sigma_\theta$  surfaces ( Fig. 5a–b, d–e ). Conversely, positive trends in temperature  
382 and salinity are most prevalent in the northeastern and/or eastern regions of the basin along the  
383 geostrophic streamlines ( Fig. 5a–b, d–e ). These patterns suggest that waters subducted in the frontal  
384 region with reduced temperature and salinity originate mainly from the northeastern North Pacific and

385 are advected southward along the subtropical circulation ( Fig. 5a–b, d–e ). Exceptions occur in parts  
386 of the northeastern basin ( 170–130°W, 40–60°N ), where warmer and more saline waters influence  
387 the water masses sinking near the Alaska gyre and subsequently transported outside the subtropical  
388 gyre and along the California coast.

389

390 At  $26.8\sigma_\theta$  ( Fig. 5g–h ), large positive trends in temperature and salinity are found along the Kuril  
391 Islands, with moderate positive trends appearing on the eastern side of the basin, respectively. Waters  
392 at this density range (  $26.8\sigma_\theta$  ) are not directly ventilated but are formed through diapycnal mixing  
393 processes [ Nakamura et al., 2000a, b; Nakamura and Awaji, 2003; You, 2003; Yasuda, 2004 ] and  
394 through double diffusion such as salt fingering [ You, 2003 ]. Thus, the observed positive temperature  
395 and salinity trends at  $26.8\sigma_\theta$  likely reflect influences from changes occurring in the overlying layers  
396 ( Fig. 5d–e and g–h ).

397

398 A meridional northward shift of the outcrop line in the North Pacific associated with recent climate  
399 change has been documented in OFES analyses [ Ogata and Nonaka, 2020 ] and in other observational,  
400 reanalysis, and eddy-resolving ocean hindcasts [ Xu et al., 2022 ]. Consistent with these studies, the  
401 present dataset exhibits clear northward migration of the  $25.0\sigma_\theta$  and  $26.0\sigma_\theta$  outcrop lines ( Fig. 6a ),  
402 with the strong shifts occurring in the eastern basin between 150°E and 180°W (Fig. 6 and Table 1).  
403 The estimated northward shift rate at  $0.004\text{--}0.09\text{ }^\circ\text{yr}^{-1}$  from 2004 to 2023 is comparable to the value of  
404  $0.04\text{ }^\circ\text{yr}^{-1}$  reported by Xu et al. [ 2022 ] for 1980 to 2018. Xu et al. [ 2022 ] further demonstrated that  
405 changes in the mixed layer and outcrop lines are tightly coupled with the northward migration of the  
406 North Pacific subtropical gyre and KE/OE fronts due to the poleward expansion of the Hadley cell,  
407 including the fact that the Kuroshio Extension and Oyashio Extension fronts, mode waters, and  
408 subtropical fronts evolve as a coherent system. These changes may also reflect the influence of

409 anthropogenic warming, which has been linked to the poleward expansion of the Hadley circulation  
410 and the associated meridional shifts of oceanic fronts [ Yang et al., 2020 ].

411

412 Such poleward displacements of frontal structures can help explain the negative temperature and  
413 salinity trends in the subtropical gyre, where less saline subarctic-origin waters are subducted and  
414 advected southward. The positive temperature and salinity trends occurring in the Alaska region  
415 [ 160°–130°W, 30°–60°N ] ( Fig. 5a–b and d–e ) are likewise consistent with the direct surface  
416 warming. In contrast, the 26.0 $\sigma_\theta$  front exhibits primarily longitudinal, rather than meridional, shifts  
417 between 2004 and 2023 ( Fig. 6 ), suggesting that the associated temperature and salinity changes arise  
418 mainly from direct surface warming and freshening, rather than from density-compensated shifts in  
419 water-mass distribution.

420

### 421 **3.3.2 Dissolved oxygen**

422 The linear trends in dissolved oxygen on the isopycnal surfaces at 25.0, 26.0, and 26.8 $\sigma_\theta$  exhibit  
423 predominantly negative values across the North Pacific ( Fig. 5c, f, and i ), although their spatial  
424 distributions are not uniform. Large negative trends are concentrated in the northeastern and eastern  
425 regions and gradually decrease toward the west ( Fig. 5c, f, and i ). Exceptions occur mainly in the  
426 tropics, where notable positive trends are found in the western tropical areas on the 26.0 and 26.8 $\sigma_\theta$   
427 surfaces.

428

429 The temporal changes in dissolved oxygen ( O<sub>2</sub> ) were decomposed following the method of Sasano et  
430 al. [ 2015 ]. The processes underlying the oxygen tendency equations ( Eqs. 2 and 3 ) are summarized  
431 below. We evaluated each contributing term and examined its relative importance for the dissolved O<sub>2</sub>  
432 trends. The total tendency of dissolved oxygen can be expressed as

433 
$$\frac{\partial O_2}{\partial t} = \left( \frac{\partial O_2}{\partial z} \frac{\partial z}{\partial t} \right) + \left( \frac{\partial O_2^{sat}}{\partial t} \right)_{net} - \left( \frac{\partial(AOU)}{\partial t} \right)_{net}, \quad (2)$$

434 which can be rearranged as

435 
$$\frac{\partial O_2}{\partial t} = \underbrace{\left( \frac{\partial O_2}{\partial z} \frac{\partial z}{\partial t} \right)}_{(i)} + \underbrace{\left( \frac{\partial O_2^{sat}}{\partial t} - \frac{\partial O_2^{sat}}{\partial z} \frac{\partial z}{\partial t} \right)}_{(iii)} + \underbrace{\left( -\frac{\partial(AOU)}{\partial t} + \frac{\partial(AOU)}{\partial z} \frac{\partial z}{\partial t} \right)}_{(v)}. \quad (3)$$

436 (i) (ii) (iii) (iv) (v) (vi)

437 Here,  $X = O_2, O_2^{sat}, AOU$  ( Apparent Oxygen Utilization ). The term  $\partial z/\partial t$  denotes the temporal  
 438 change in the depth of the isopycnal surface (z), while  $\partial X/\partial z$  represents the vertical gradient of the  
 439 variable  $X$  at that surface, averaged over the past 20 years. The net tendency term  $(\partial X/\partial t)_{net}$   
 440 represents the net changes associated with a variable X.

441

442 By applying Eq. ( 3 ), the rate of  $O_2$  change ( term i ), which is the rate of reconstructed  $O_2$  data  
 443 estimated from the linear regression analysis, on each isopycnal surface can be decomposed into  
 444 contributions from:

445 ( term ii ) vertical heave acting on the vertical  $O_2$  gradient;

446 ( term iii ) solubility effects due to temperature and salinity changes;

447 ( term iv ) vertical heave acting on the solubility gradient;

448 ( term v ) AOU changes related to air-sea disequilibrium, biological activities, and lateral circulation

449 ( term vi ) vertical heave acting on AOU gradients.

450 The derivation of Eqs. ( 2 ) and ( 3 ) follows Sasano et al. [ 2015 ] and is described in Appendix. A  
 451 schematic illustration of this decomposition is provided in Supplementary Figure S5.

452

453 Figure 7 shows the horizontal distributions of the magnitude of each term on 25.0, 26.0, and 26.8 $\sigma_\theta$   
454 surfaces. The results indicate that the prominent O<sub>2</sub> declines ( Fig. 5c, f, i ) arise from a combination  
455 of positive and negative contributions, with the dominant terms varying by latitude. In the high-latitude  
456 region around the Alaska Gyre ( 170°–130°W, 40°–60°N ), the largest negative contributions are  
457 associated with the deepening of isopycnal surfaces ( term ii ) and the vertical heave acting on the  
458 AOU gradient ( term vi ) ( Fig. 7f, j, k, o ). Because the dissolved oxygen generally decreases with  
459 depth (  $\partial O_2 / \partial z < 0$  ), deepening of isopycnal surfaces (  $\partial z / \partial t > 0$  ) ( Fig. 8 b–c ) produces a  
460 negative contribution through vertical heave. Similarly, because AOU typically increases with depth,  
461 isopycnal deepening leads to an apparent increase in AOU, contributing negatively to dissolved O<sub>2</sub> via  
462 term ( vi ). In contrast, solubility-related changes ( term iii ) and net AOU tendencies ( term v ) act in  
463 opposite directions during this period ( Fig. 7g–h, l–m ). Taken together, these results are consistent  
464 with the strong negative O<sub>2</sub> trends observed in the Bering Sea on the 26.0 $\sigma_\theta$  and 26.8 $\sigma_\theta$  surfaces  
465 ( 150°E–170°W, 50–60°N; Figs. 5f and i ).

466

467 In the subtropical and mid-latitudes ( 10°–40°N ), the O<sub>2</sub> decline is largely associated with AOU  
468 changes ( term v ) ( Fig. 7d, i, and n ). The relative weakening of the total O<sub>2</sub> decrease in the western  
469 North Pacific ( Fig. 5c, f, i ) coincides with positive contributions from vertical heave of isopycnal  
470 surfaces ( term ii ) ( Fig. 7f and k ). Additional positive trends arise from solubility-related effects  
471 ( term iii ) ( Fig. 7b ), and the vertical heave acting on the AOU gradient ( term vi ) ( Fig. 7j and o and  
472 Fig. 8b–c ).

473

474 In the mid-ocean between 170°E and 160°W, the positive O<sub>2</sub> tendencies transition to weakly negative  
475 values. In contrast, a pronounced band of positive trends is found zonally across the North Pacific

476 Ocean between 30°N and 50°N, primarily associated with the combined effects of terms ( iii ) and ( v )  
477 ( Fig. 7l, h–i, and m–n ). This pattern may be related to the northward meridional shift of the subtropical  
478 and subarctic frontal zone under recent global warming [ Ogata and Nonaka, 2020 ]. Enhanced winter  
479 convection in this region may introduce nutrients into the surface layer, potentially increasing  
480 biological activity and AOU. In the NPIW formation region near the Kuril Islands, negative  
481 contributions from term ( iii ) are observed ( Fig. 7l ), suggesting weaker vertical mixing during the  
482 observational period, likely influenced by enhanced surface-layer stratification. This interpretation is  
483 supported by the positive trends in temperature and salinity observed in the winter subducted areas  
484 [ Suga et al., 1997; 2004; Yasuda, 2004 ] ( Fig. 5d–e, g–h ).

485

486 In the western tropical Pacific, pronounced increases in dissolved O<sub>2</sub> are observed within the density  
487 range of 26.8–27.2  $\sigma_{\theta}$  ( Fig. 3c and g; Fig. 4c and g; Fig. 5c, f, and i ), overlapping with the OML  
488 [ Reid, 1997 ]. Similar features have been reported by Sasano et al. [ 2015 ] and Takatani et al. [ 2012 ].  
489 Variability of the North Equatorial Counter Current ( NECC ) is likely relevant in this region.  
490 According to the study of Chen et al. [ 2016 ] based on the OFES outputs including a multidecadal  
491 variability (1960–2014), the NECC exhibits two distinct modes of variability: an interannual mode  
492 characterized by strengthening accompanied by southward migration, and an interdecadal mode  
493 marked by a gradual weakening, poleward migration, and broadening.

494

495 The validity of time-varying signals in the western tropical Pacific in the OFES data has been  
496 demonstrated by Chen et al. [ 2016 ]. We further examined the longer-term OFES data ( 1950–2023 ),  
497 as well, for poleward, eastward velocities, as well as potential temperature and salinity here ( Fig. 9c,  
498 g ). Positive temperature anomalies in 0°–5 °N occur above 250 m depth, while negative anomalies

499 appear along the  $26.0\sigma_\theta$  surface between  $5^\circ$ – $20^\circ$ N, a similar pattern that is also evident in the GOBAI-  
500  $O_2$  data ( Fig. 3a ). A discrepancy is found in salinity trends: GOBAI- $O_2$  shows negative trends along  
501  $26.0\sigma_\theta$  ( Fig. 3b ), whereas OFES exhibits positive trends ( Fig. 9b, f ), likely reflecting higher salinity  
502 at 200–600 m depth in OFES between  $0^\circ$  and  $7^\circ$ N ( Fig. 10b, d ).

503

504 Anomalies in poleward and eastward velocities ( Fig. 9a–b, e–f and Fig. 11a–b ) indicate enhanced  
505 poleward flow around  $5^\circ$ N above 200m depth and a poleward shift of the eastward velocity core. These  
506 changes are consistent with the interdecadal mode of NECC variability described by Chen et al.  
507 [ 2016 ]. The broadening of the NECC was less evident here, possibly because the present analysis  
508 uses raw velocity fields rather than isolating the second EOF modes. The wind-stress curl over the  
509 equatorial Pacific shows a persistent decrease and poleward expansion of negative values along the  
510  $0^\circ$ – $10^\circ$ N from 1950 to 2023 ( Fig. 12 ).

511

512 The westward penetration of the OML is slow and occurs between two eastward-extending tongues of  
513 high  $O_2$  water originating near the equator [ Reid, 1997 ] (Fig. S6). The observed  $O_2$  increase on the  
514  $26.8$ – $27.2 \sigma_\theta$  surfaces ( Fig. 3c, g and Fig. 4c, g ) is consistent with a weakening and northward shift  
515 of the interdecadal NECC mode. The subsurface  $O_2$  increase, particularly below 400m depth ( Fig. 1r–  
516 u ), is therefore likely influenced by these circulation changes, potentially allowing higher- $O_2$  water to  
517 extend westward ( Fig. S6 ). In addition, shoaling of isopycnal surfaces near the equator indicates a  
518 northward shift of the boundary between the tropical and subtropical gyres along  $137^\circ$ E line during  
519 the observational period.

520

521

#### 522 **4. Discussion and Conclusion**

523 The variability of dissolved oxygen in the North Pacific reflects the combined influences of global  
524 warming and climate variability. In this study, we used the four-dimensional GOBAI-O<sub>2</sub> dataset,  
525 constructed using machine-learning methods applied to historical temperature, salinity, and oxygen  
526 observations from BGC-Argo floats and ship-based measurements—to examine linear trends in  
527 potential temperature, salinity, and dissolved oxygen over the past two decades ( 2004–2023 ). The  
528 linear trends are broadly consistent with findings from previous studies [ Takatani et al. 2012; Sasano  
529 et al. 2015; Ogata and Nonaka, 2020 ], and we clarified how these trends vary spatially ( Figs. 3 and  
530 4 ).

531

532 An important outcome of this study is that GOBAI-O<sub>2</sub>, being globally gridded, allows spatially  
533 continuous and smooth representations of trends, both horizontally and vertically, across the North  
534 Pacific. This provides a more spatially coherent representation than earlier datasets that relied solely  
535 on sparse ship-based observations. The horizontal trend patterns mapped on isopycnal surfaces ( Fig.  
536 5 ) show that dissolved oxygen exhibits a basin-scale decreasing trend. At the same time, several  
537 regions display locally increasing oxygen, including areas influenced by the meridional migration of  
538 subtropical and subpolar fronts ( Fig. 4 ). The strong positive oxygen trends in the western equatorial  
539 region are consistent with a weakening of the second mode of the NECC variability. The  
540 decomposition analysis further illustrates how each physical component contributes to oxygen changes  
541 along isopycnal surfaces ( Fig. 7 ).

542

543 Although many of the large-scale features identified here resemble those reported by Ito et al. [ 2017 ],  
544 our analysis reveals regional and isopycnal-scale structures that were previously unresolved. In

545 particular, the positive oxygen trends in the Kuroshio–Oyashio Transition Zone, the northeastern North  
546 Pacific along the 26.8–27.0  $\sigma_\theta$  density surfaces, and the enhanced subsurface O<sub>2</sub> increase in the tropical  
547 western Pacific below 400 m were not clearly distinguished in earlier O<sub>2</sub> anomaly studies. These  
548 improvements arise because GOBAI-O<sub>2</sub> integrates high-frequency BGC-Argo oxygen observations  
549 with a spatially consistent mapping scheme, reducing observational gaps and sampling biases in  
550 dynamically active regions. This suggests that regional reoxygenation signals can coexist with large-  
551 scale deoxygenation, and highlights the importance of sustained BGC-Argo observations for detecting  
552 emerging changes in ocean biogeochemistry.

553

554 Recent work by Bushinsky et al. [ 2025 ] has reported the presence of a systematic negative bias  
555 (approximately -2.7  $\mu\text{mol kg}^{-1}$ ) in air-calibrated BGC-Argo oxygen measurements compared with  
556 ship-based reference profiles. This bias does not appear to be explicitly corrected in version 4.4 of  
557 GOBAI-O<sub>2</sub>-v2.2 and may therefore influence the magnitude of the estimated oxygen trends—  
558 potentially enhancing negative trends or suppressing positive ones in regions with dense float sampling.  
559 However, as described in Section 2.1, a substantial fraction of these float data is subject to quality  
560 control through comparison with climatological fields derived from ship-based discrete observations,  
561 and only profiles with appropriate quality flags are retained and incorporated into the dataset  
562 development. While this filtering procedure likely mitigates a portion of the air-calibration bias, the  
563 extent to which residual bias remains in the reconstructed fields is not well quantified.

564

565 If present, such biases could also affect the apparent vertical structure of the oxycline. In the North  
566 Pacific, regions with high float density—such as the Kuroshio–Oyashio transition zone, the North  
567 American coastal region, and the vicinity of Hawaii—may be particularly affected (see Fig. 1 of Sharp  
568 et al., 2023). While a constant offset would not directly alter linear trend estimates, any time-varying

569 bias associated with sensor behavior or sampling depth could introduce spurious trends. A quantitative  
570 evaluation is not feasible at present due to the lack of temporally continuous ship-based reference data  
571 at the spatial scales. This limitation should therefore be kept in mind when interpreting the O<sub>2</sub> trends  
572 reported here. Accordingly, the interpretation of the diagnosed O<sub>2</sub> trends should be made with caution,  
573 particularly in regions where float-based observations dominate.

574

575 It is also essential to recognize that GOBAI-O<sub>2</sub> is a machine learning reconstruction derived from  
576 available temperature, salinity, and oxygen measurements. While this approach significantly enhances  
577 spatial coverage, the results should be interpreted cautiously. In particular, although the large-scale  
578 spatial patterns are broadly consistent across datasets, both the magnitude of trends and finer-scale  
579 spatial features may still be affected by unresolved observational and reconstruction uncertainties.  
580 Nevertheless, future work incorporating improved calibration of Argo oxygen sensors, expanded ship-  
581 based reference datasets, independent machine learning reconstructions [ e.g., Ito et al., 2024 ], and  
582 comprehensive ocean reanalysis will be necessary to better constrain these uncertainties.

583

584 Different versions of the GOBAI-O<sub>2</sub> product may yield different oxygen trend estimates because of  
585 methodological differences among releases. Therefore, some of the regional patterns discussed in this  
586 study may be sensitive to the specific GOBAI-O<sub>2</sub> version used in the analysis. Future comparisons  
587 across multiple GOBAI-O<sub>2</sub> versions and observational products would help further assess the  
588 robustness of the results.

589

590 The monthly mean climatological GOBAI-O<sub>2</sub> dataset should include the Pacific Decadal Oscillation  
591 ( PDO; Stramma et al., 2020; Pozo Buil and Di Lorenzo, 2017 ) and the North Pacific Gyre Oscillation  
592 ( NPGO; Stramma et al., 2020 ). This dataset, therefore, provides a valuable basis for examining how

593 such climate variability influences dissolved oxygen through physical driving mechanisms.  
594 Investigating these relationships more explicitly will be an important direction for future research.

595

596

597 **Data availability:**

598 GOBAI-O<sub>2</sub> data is available at [https://www.ncei.noaa.gov/access/metadata/landing-](https://www.ncei.noaa.gov/access/metadata/landing-page/bin/iso?id=gov.noaa.nodc:0259304)  
599 [page/bin/iso?id=gov.noaa.nodc:0259304](https://www.ncei.noaa.gov/access/metadata/landing-page/bin/iso?id=gov.noaa.nodc:0259304). Temperature and salinity are from Roemmich and Gilson  
600 [ 2009] Argo climatology ( [https://sio-argo.ucsd.edu/RG\\_Climatology.html](https://sio-argo.ucsd.edu/RG_Climatology.html) ). The OFES, NCEP-  
601 NCAR, and GODAS data used in our study are obtained from APDRC, University of Hawaii  
602 ( <http://apdrc.soest.hawaii.edu> ).

603

604 **Author contributions:**

605 MI designed the study, performed the analyses, and prepared all figures. MI wrote the initial draft of  
606 the manuscript. MI and TO contributed to the interpretation of the results. All authors contributed to  
607 improving the manuscript.

608

609 **Acknowledgements:**

610 Jonathan D. Sharp and the reviewers are acknowledged for providing comments that prompted  
611 significant improvements to this manuscript.

612

613 **Competing interests:** The authors declare no competing interests.

614

615 **Financial support:**

616 This research has been supported by the Institute for Basic Science (grant no. IBS-R028-D1) and the

617 Japan Society for the Promotion of Science (JSPS) through a Grant-in-Aid for Scientific Research  
618 JP22H00176.

619

620

621

622

623

624

625

626

627

628

629 **Table captions:**

630 Table 1. Northern shifts of the (outcrop) isopycnal latitudes ( $^{\circ} \text{yr}^{-1}$ ) for  $25.0\sigma_{\theta}$  (a),  $26.0\sigma_{\theta}$  (b), and  
631  $26.8\sigma_{\theta}$  (c) in the GOBAI-O<sub>2</sub>, OFES, and GODAS datasets. The estimates are based on data from March  
632 of each year. For  $26.8 \sigma_{\theta}$ , the northern shift is evaluated using the isopycnal depths corresponding to  
633 182, 178m, and 183m in GOBAI-O<sub>2</sub>, OFES, and GODAS, respectively.

634 (a)  $25.0\sigma_{\theta}$

<b>Longitude</b>	<b>GOBAI-O<sub>2</sub></b>	<b>OFES</b>	<b>GODAS</b>
<b>150 °E</b>	0.0241	0.0157	0.0283
<b>170 °E</b>	0.0444	0.0052	0.0240
<b>170 °W</b>	0.0684	0.0871	0.0481
<b>150 °W</b>	0.0947	0.0353	0.0313

635	<b>130 °W</b>	0.0420	0.0471	0.0121
	(b) 26.0 $\sigma_\theta$			
	<b>Longitude</b>	<b>GOBAI-O<sub>2</sub></b>	<b>OFES</b>	<b>GODAS</b>
	<b>150 °E</b>	0.0368	0.0766	0.0358
	<b>170 °E</b>	0.0436	-0.0305	0.0508
	<b>170 °W</b>	0.0124	0.1997	0.1412

636 (c)26.8 $\sigma_\theta$

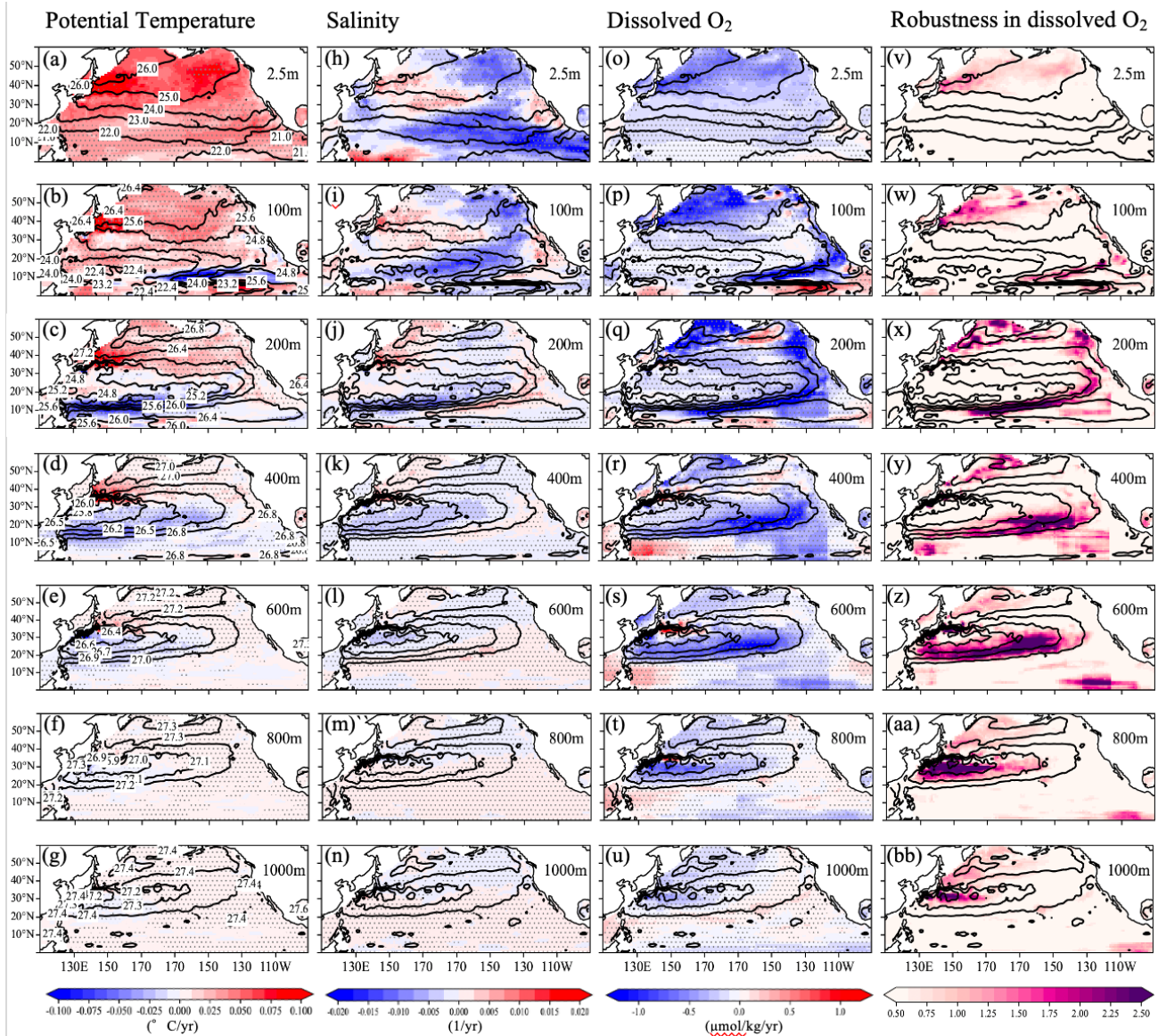
	<b>Longitude</b>	<b>GOBAI-O<sub>2</sub></b>	<b>OFES</b>	<b>GODAS</b>
	<b>150 °E</b>	0.0371	0.1980	0.0046
	<b>170 °E</b>	0.0338	0.0217	0.1637
	<b>170 °W</b>	0.0728	0.0054	0.0261

637

638

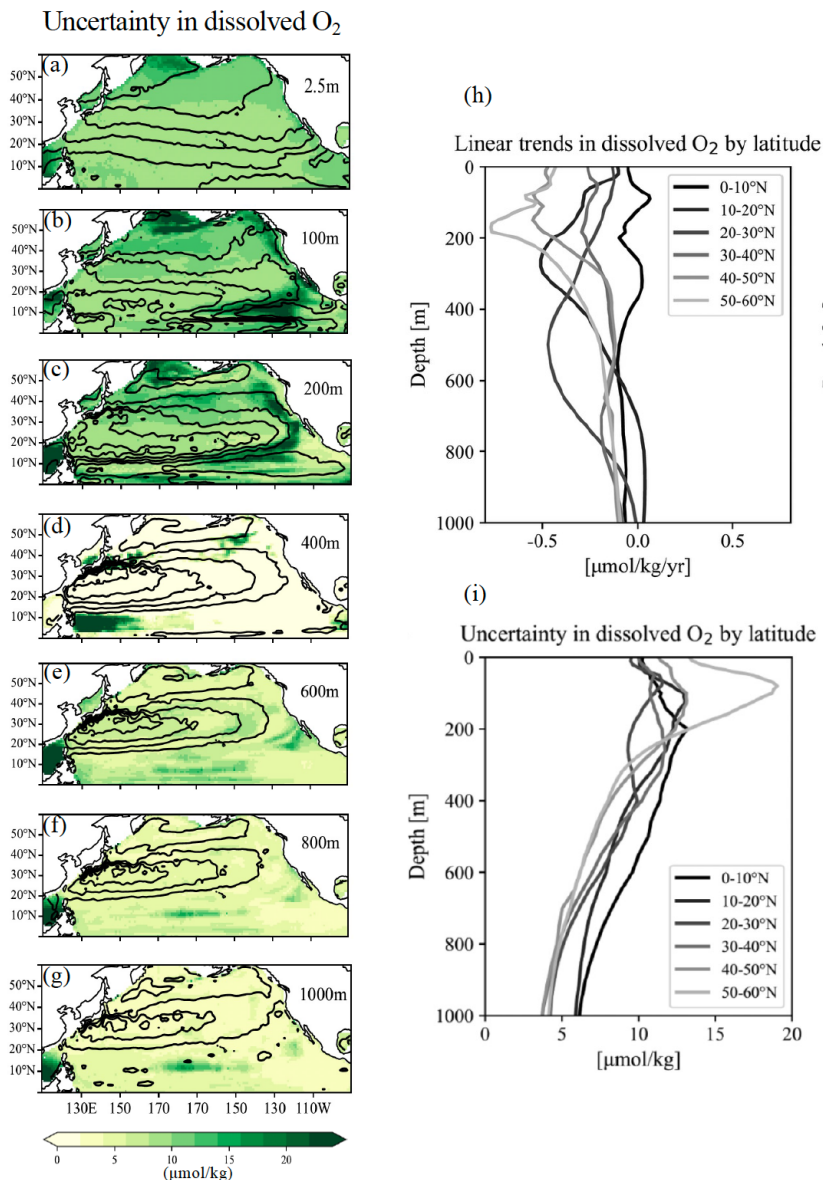
639 **Figure captions:**

640



641

642 **Figure 1** Horizontal distributions of linear trends in ( a–g ) potential temperature, ( h–n ) salinity, and  
 643 ( o–u ) dissolved oxygen (  $O_2$  ) during the observational period at depths of 0, 100, 200, 400, 600, 800,  
 644 and 1000 m, respectively. Hatched areas indicate statistically significant trends at the 95% confidence  
 645 level based on a Student’s t-test with effective degrees of freedom accounting for temporal  
 646 autocorrelation. Trend significance was evaluated using a Student’s t-test with effective degrees of  
 647 freedom accounting for lag-1 autocorrelation. Contours denote potential density at each depth. Labels  
 648 for the potential density are shown only in the potential temperature sections. Corresponding  
 649 distributions of the Robustness (  $R$  ), defined as the ratio of the trend magnitude to the dataset  
 650 uncertainty in dissolved  $O_2$  are presented in panels ( v–bb ).  
 651

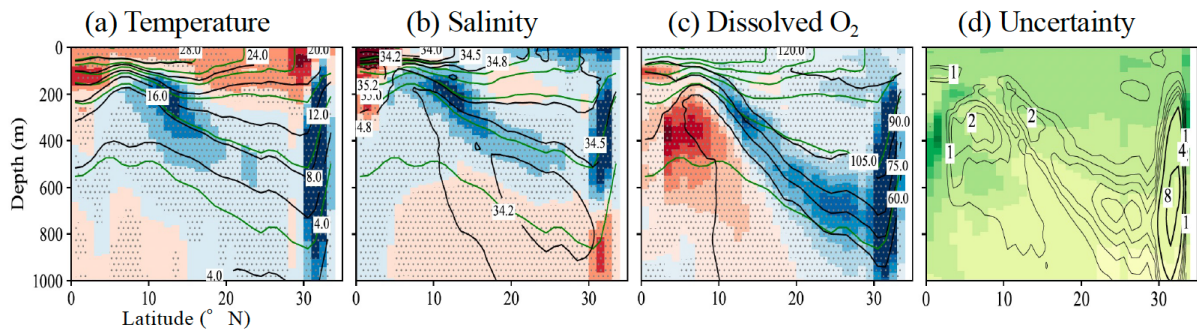


652

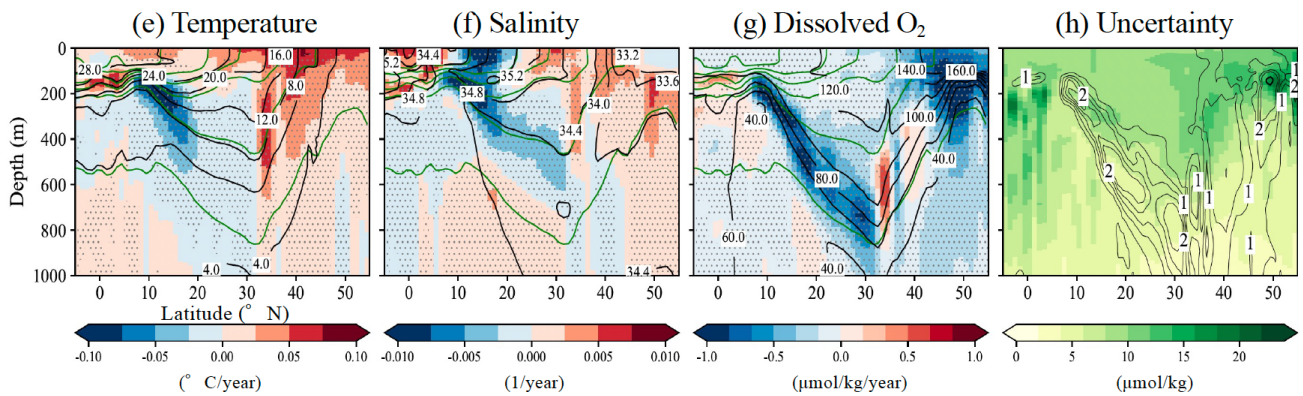
653 **Figure 2** Horizontal distributions of dataset uncertainty in dissolved O<sub>2</sub> ( a–g ) and vertical profiles of  
 654 linear trends and uncertainty in dissolved O<sub>2</sub> by latitude ( h–i ).

655

137° E line



165° E line

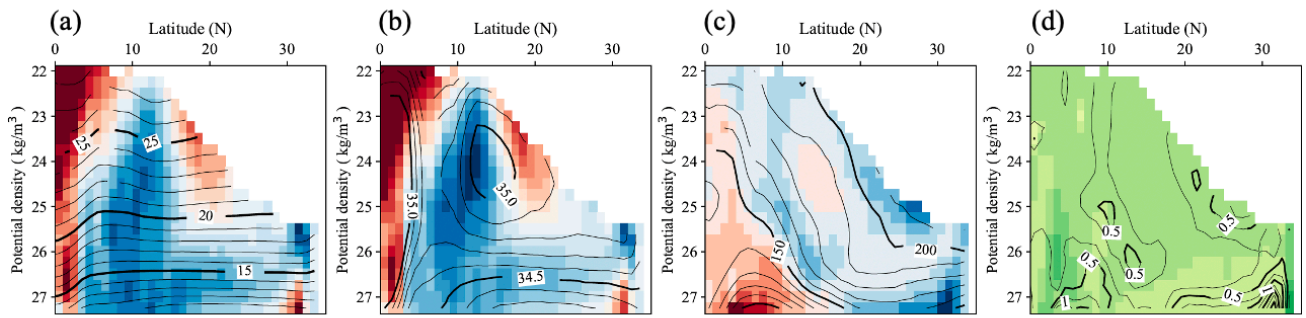


656

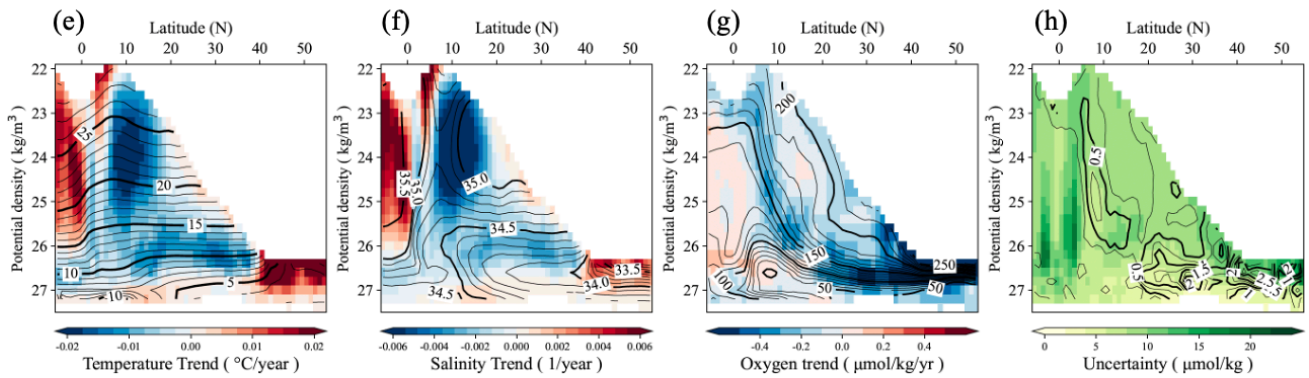
657 **Figure 3** Vertical sections showing linear trends in potential temperature ( a, e ), salinity ( b, f ), and  
658 dissolved O<sub>2</sub> ( c, g ) along the 137°E and 165°E meridians, respectively. Black contour lines indicate  
659 the mean potential temperature ( a, f ), salinity ( b, g ), and dissolved oxygen ( c, h ) over the period  
660 2004–2023, while green contour lines represent the mean potential density. Labels for the potential  
661 density are shown only in the robustness sections. Hatched areas indicate statistically significant trends  
662 at the 95% confidence level based on a Student’s t-test with effective degrees of freedom accounting  
663 for temporal autocorrelation. Trend significance was evaluated using a t-test with effective degrees of  
664 freedom accounting for lag-1 autocorrelation. Corresponding vertical sections of the mean uncertainty  
665 with the contours of the Robustness ( R ) in panels ( d, h ). The contour intervals for thin and thick  
666 contours in ( d, h ) are 0.5 and 4.0, respectively.

667

## 137° E Line



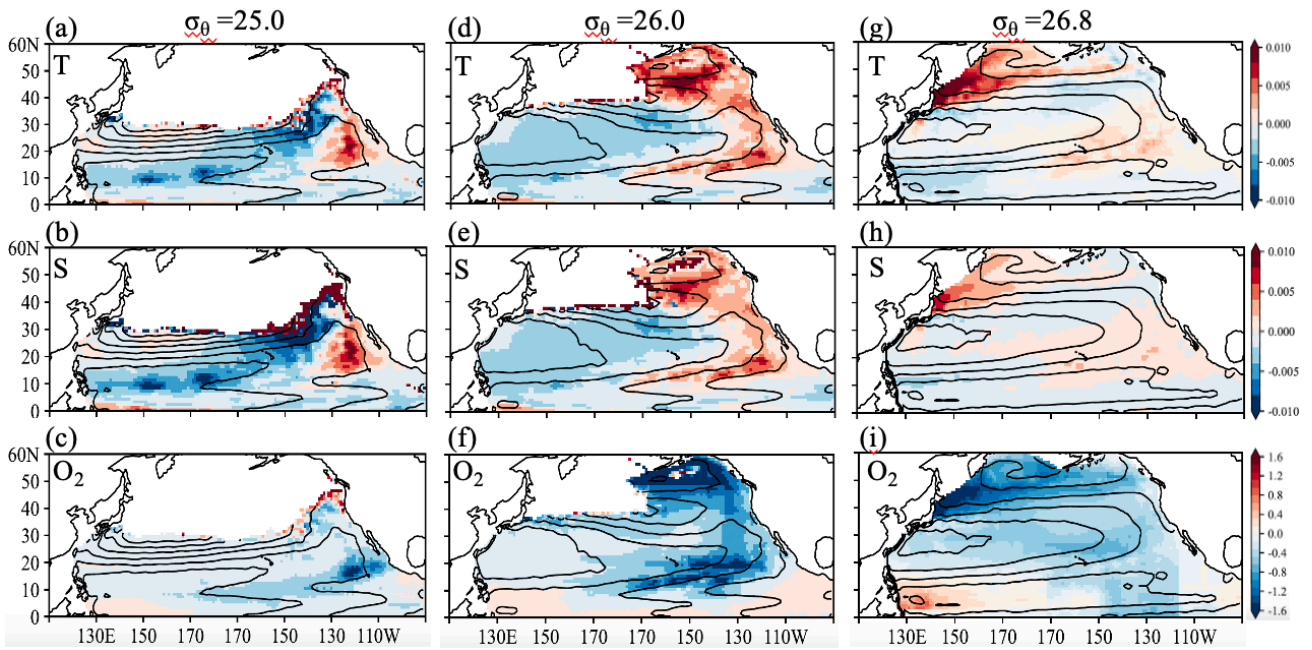
## 165° E Line



668

669 **Figure 4** Linear trends in ( a, e ) potential temperature, ( b, f ) salinity, ( c, g ), and dissolved  $\text{O}_2$  on  
 670 each isopycnal surface at intervals of  $0.1\sigma_{\theta}$ , calculated at every 1.0 deg of latitude in 137 °E and 165 °E  
 671 lines, respectively. Contour lines represent the mean values during the target observation periods,  
 672 plotted at intervals of  $0.1\sigma_{\theta}$  for each 1 degree of latitude. Panels ( d, h ) show the corresponding vertical  
 673 sections of mean uncertainty, along with contours of robustness (R). The contour intervals for thin and  
 674 thick contours in (d, h) are 0.25 and 0.5, respectively.

675

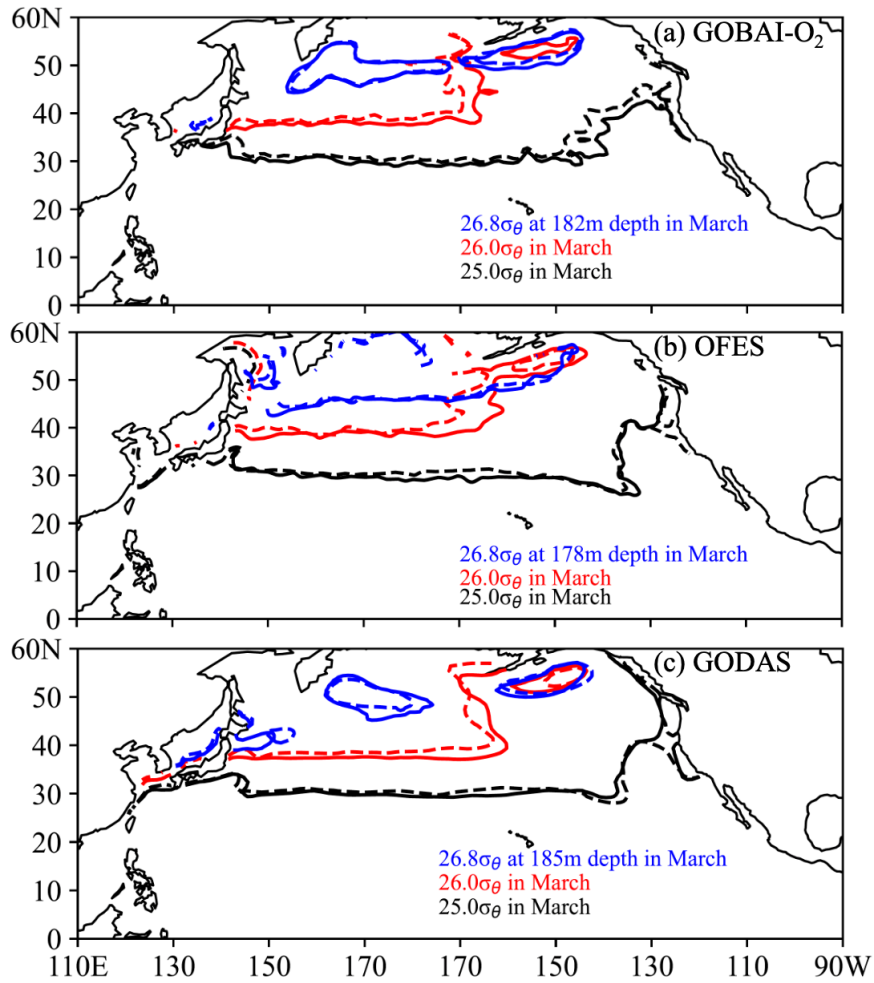


676

677 **Figure 5** Linear trends in ( a ) potential temperature ( °C/yr ), ( b ) salinity ( 1/yr ), and ( c ) dissolved  
 678 O<sub>2</sub> ( μmol/kg/yr ) on each isopycnal surface at 25.0, 26.0, and 26.8σ<sub>θ</sub>. Contour lines represent geostrophic  
 679 flow streamlines on 26.0 and 26.8σ<sub>θ</sub> surfaces, relative to 2000 m.

680

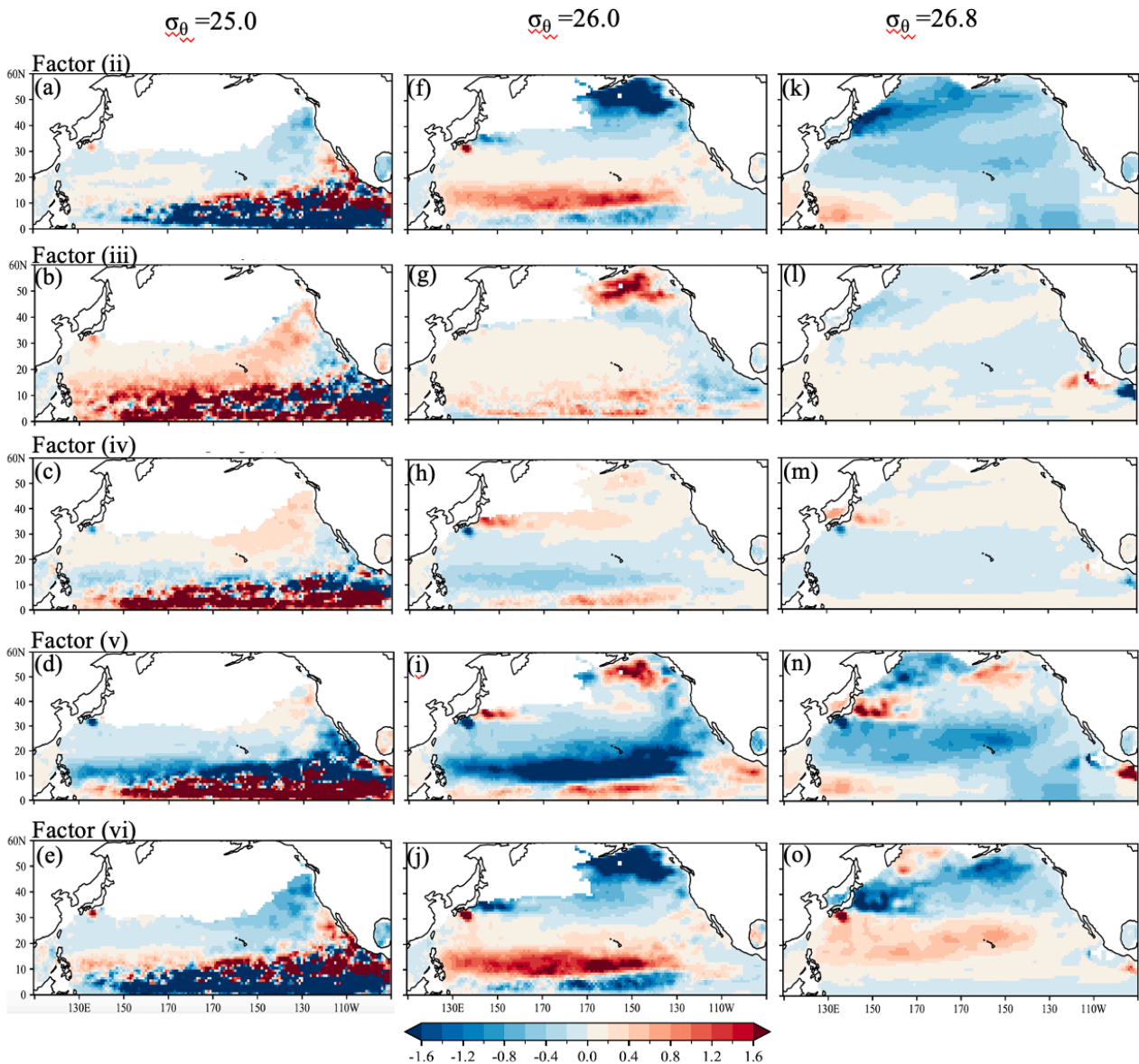
681



682

683 **Figure 6** Density contours of  $25.0\sigma_\theta$  ( black ),  $26.0\sigma_\theta$  ( red ), and  $26.8\sigma_\theta$  ( blue ) in each dataset: (a)  
 684 GOBAI- $O_2$ , (b) OFES, and (c) GODAS. Solid lines indicate the mean March density contours for  
 685 2004–2009, while dashed lines represent those for 2019–2023.

686

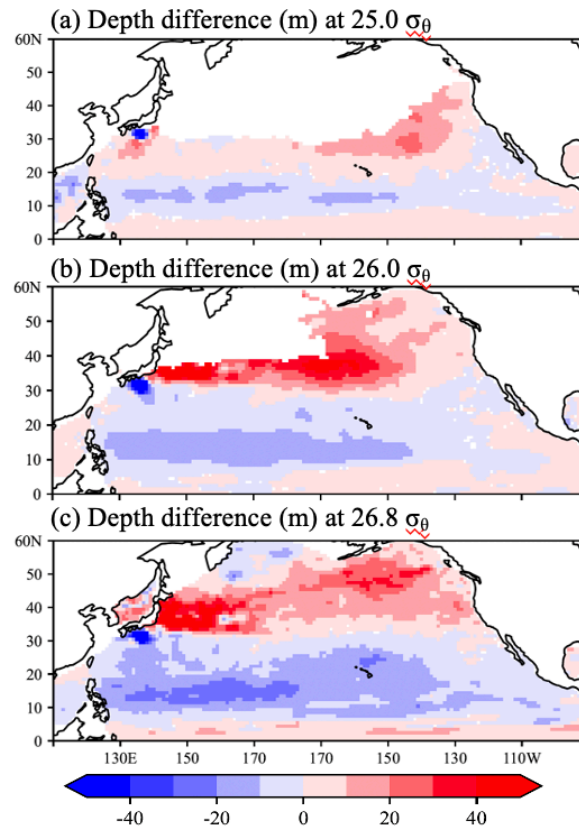


687

688 **Figure 7** Horizontal distributions of the changing rates ( $\mu\text{mol/kg/yr}$ ) of each factor contributing to the  
 689 rate of  $\text{O}_2$  change on 25.0, 26.0, and 26.8  $\sigma_{\theta}$  in Eq. ( 1 ). The rate of  $\text{O}_2$  change on each isopycnal  
 690 surface is decomposed into the following components: ( ii ) the apparent contribution from vertical  
 691 heave (deepening or shoaling) of isopycnal surfaces associated with warming and/or surface  
 692 freshening; ( iii ) the contribution from changes in oxygen solubility (  $\text{O}_2^{\text{sat}}$  ) associated with  
 693 temperature and salinity variations; ( iv ) the contribution from vertical heave acting on the background  
 694 solubility gradient; ( v ) the contribution from net changes in apparent oxygen utilization ( AOU )  
 695 associated with air–sea disequilibrium, biological activity, and lateral advection and/or circulation; and  
 696 ( vi ) the contribution from vertical heave acting on AOU gradients, independent of solubility changes.  
 697 This decomposition is applied to the reconstructed dissolved oxygen fields obtained from linear

698 regression analysis.

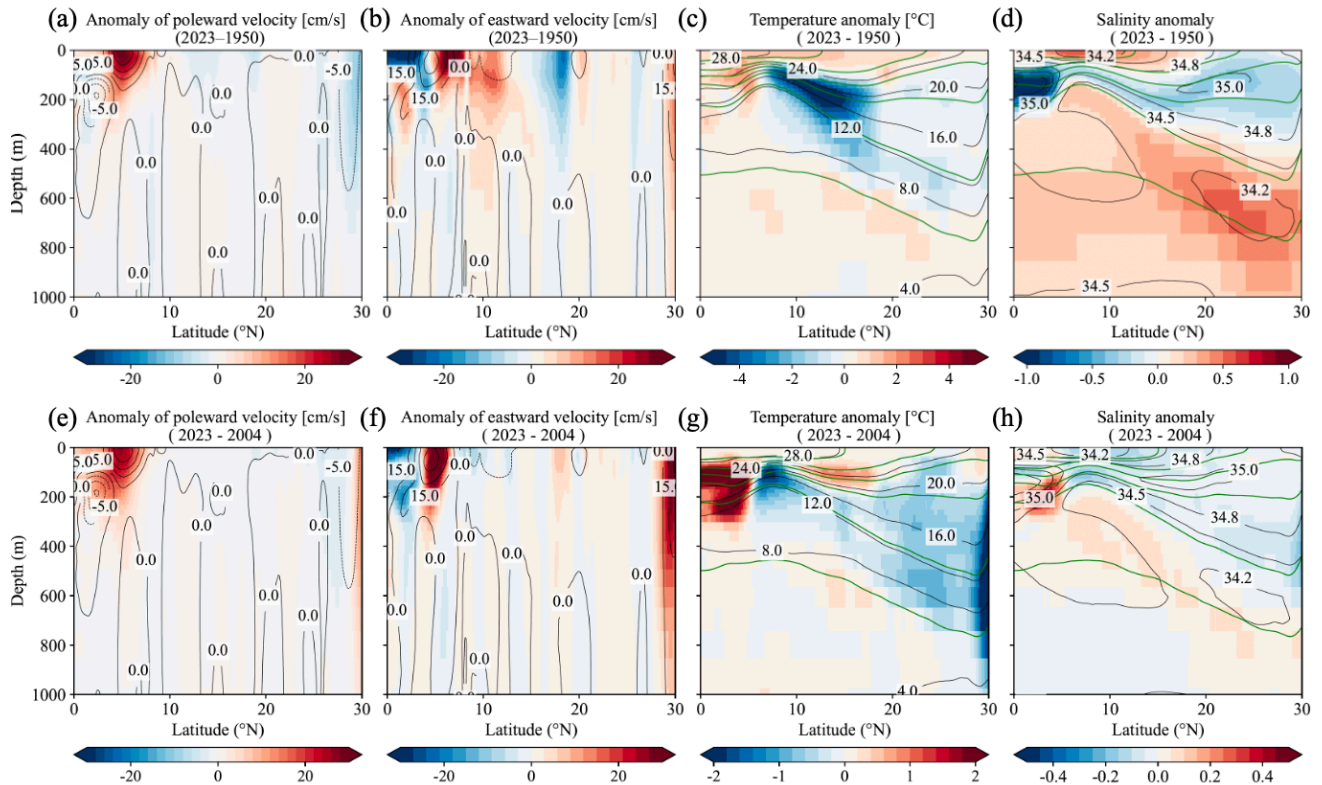
699



700

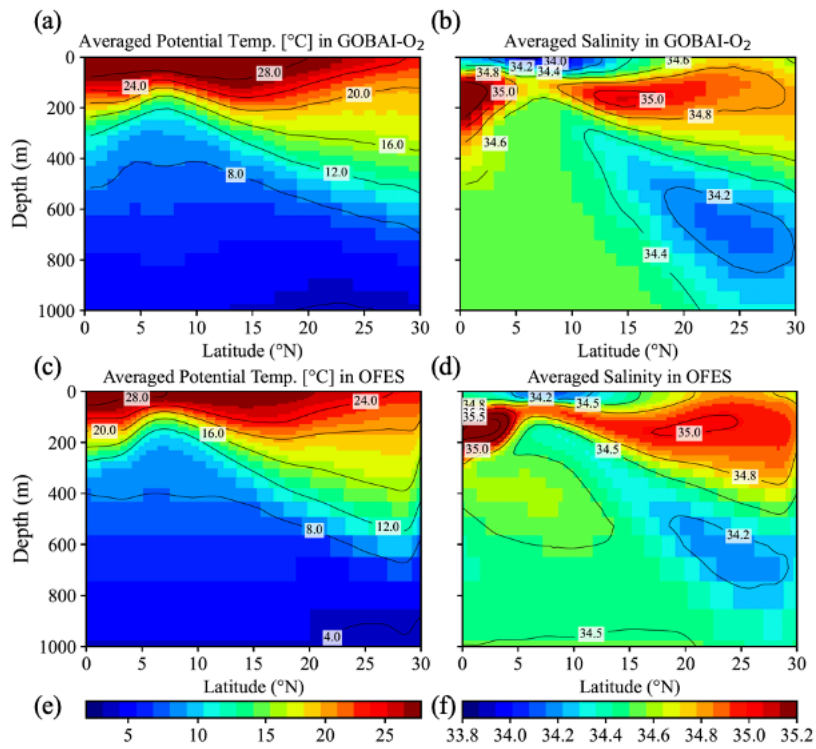
701 **Figure 8** Depth difference ( m ) between the 5-year averaged data in March, 2004–2009 and 2018–  
702 2023 at 25.0, 26.0, and 26.8 $\sigma_{\theta}$ . The reconstructed O<sub>2</sub> data estimated from the linear regression analysis  
703 were used in this calculation. Positive and negative values indicate the deepening and shallowing,  
704 respectively, from the depth of each density in 2004–2023.

705



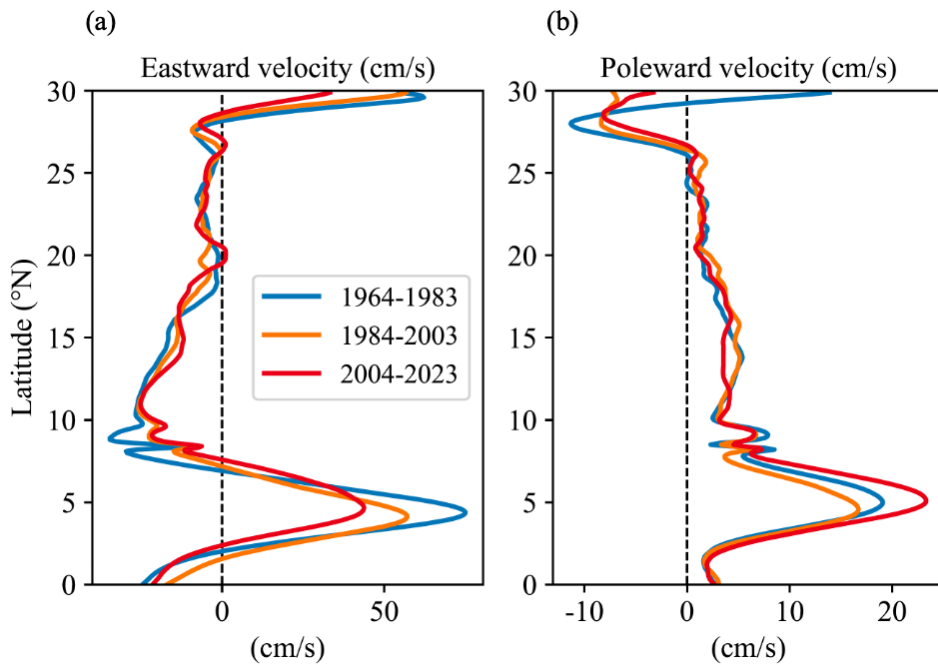
706

707 **Figure 9.** Anomaly of poleward and eastward velocity, potential temperature, and salinity in the OFES  
 708 model outputs from 1950 to 2023 ( a–d ) and from 2004 to 2023 ( e–h ), respectively, in the 137°E line.  
 709 Contours of averaged values of poleward and eastward velocity, potential temperature, and salinity  
 710 during the target period are also shown in each figure. Green contour lines in ( c–d, g–h ) indicate the  
 711 average potential density of 22, 23, 24, 25, 26, and 27 $\sigma_{\theta}$ , during the target periods.



712

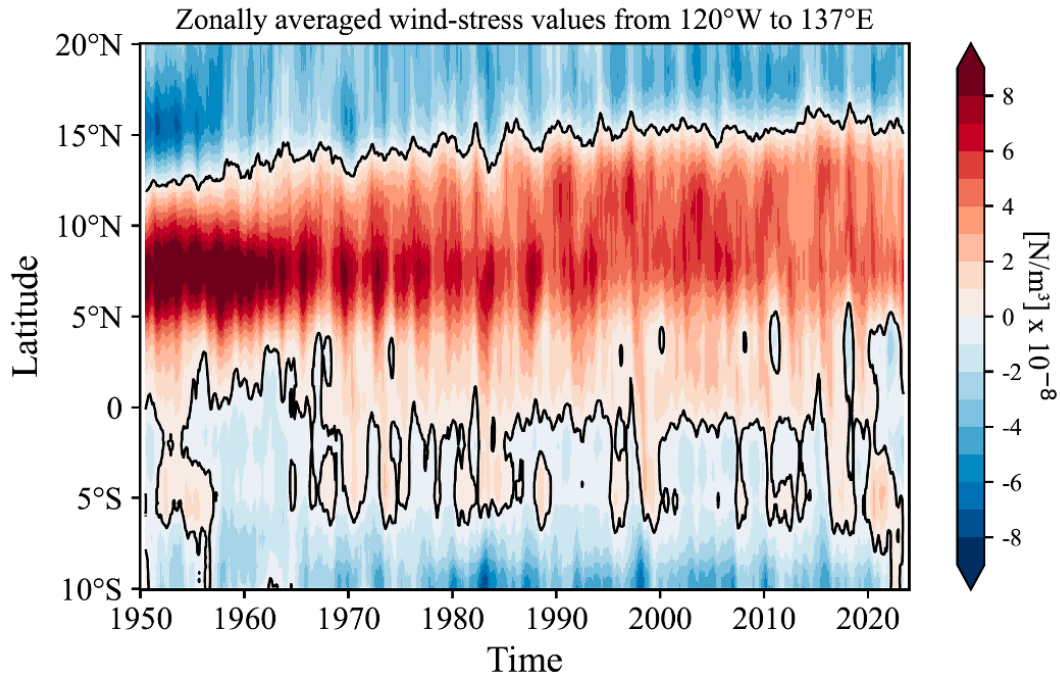
713 **Figure 10.** Averaged Potential Temperature ( a, c ) and salinity ( b, d ) in GOBAl-O<sub>2</sub> from 2004 to  
 714 2023 and OFES data from 1950 to 2023, respectively, in the 137°E line.



715

716 **Figure 11.** Latitudinal distribution of averaged eastward ( a ) and poleward velocity ( b ) in the OFES  
 717 data from 1964 to 1983, from 1984 to 2003, and from 2004 to 2023, respectively, in the 137°E line.

718



719

720 **Figure 12.** NCEP-NCAR wind-stress curl values zonally averaged from 137°E to 120° W from 1950  
 721 to 2023. A 13-month running-mean filter has been applied in time.

722

723 **Appendix: Essential concepts and derivations for Equation ( 2–3 )**

724 The essential concepts and derivations for equations ( 2 ) and ( 3 ) were originally proposed by Takatani  
 725 et al. [ 2012 ] and subsequently described in detail by Sasano et al. [ 2015 ]. Here, we briefly summarize  
 726 and follow their derivation.

727

728 When the temperature at a depth  $z_A$  increases from  $\theta_A$  to  $\theta_A'$  as a result of increased ocean heat  
 729 content, the density at that depth decreases from  $\sigma_A$  to  $\sigma_A'$ . For simplicity, the vertical salinity profile  
 730 is assumed to remain unchanged with time. As a consequence, the isopycnal surface of  $\sigma_A$  deepens  
 731 from  $z_A$  to  $z_B$  ( Figure S5 ). If surface freshening occurs simultaneously due to a net freshwater input,  
 732 both the density decreases at  $z_A$  ( from  $\sigma_A$  to  $\sigma_A'$  ) and the deepening of the isopycnal surface ( from  
 733  $z_A$  to  $z_B$  ) are enhanced. Because density is a function of temperature and salinity (  $\sigma = f(\theta, S)$  ), the

734 density of the isopycnal surface  $\sigma_A$  can be expressed as

735 
$$\sigma_A = f(\theta_A, S_A) \quad (\text{before warming}) \quad (\text{C1})$$

736 
$$= f(\theta_B', S_B). \quad (\text{after warming}) \quad (\text{C2})$$

737 Here,  $S_A$  and  $S_B$  denote salinity at depth  $z_A$  and  $z_B$ , respectively, and  $\theta_B'$  represents the temperature at  
738 density  $\sigma_A$  at depth  $z_B$  after warming. The depth  $z_B$  is determined by satisfying Eqs. (C1) and (C2).  
739 In the region where salinity decreases with depth ( e.g., above the salinity minimum layer of NPIW ),  
740  $S_A > S_B$ , and therefore  $\theta_A > \theta_B'$ . This implies that the potential temperature on an isopycnal surface  
741 effectively decreases as a consequence of warming, and that biogeochemical properties on the same  
742 isopycnal surface are also expected to change.

743

744 For a tracer  $X$  whose vertical profile with respect to depth does not change with time ( e.g., salinity;  
745 see Figure S5 ( c ) ), the temporal change of  $X$  on the potential density surface  $\sigma_A$  is attributed solely  
746 to the apparent change caused by the deepening of the isopycnal surface from  $z_A$  to  $z_B$ :

747 
$$\frac{\partial X}{\partial t} = \left( \frac{\partial X}{\partial z} \cdot \frac{\partial z}{\partial t} \right) \quad (\text{C3})$$

748 Here,  $\partial X/\partial t$  represents the temporal change of  $X$  observed on  $\sigma_A$  ( gray arrows in Figure S5 ),  $z$   
749 denotes the depth of  $\sigma_A$ ,  $\partial X/\partial z$  is the vertical gradient of  $X$  with respect to the depth ( assumed to be  
750 time-invariant ), and  $\partial z/\partial t$  is the rate of deepening of the isopycnal surface  $\sigma_A$ . The product  
751  $\partial X/\partial z \cdot \partial z/\partial t$  represents the effect of isopycnal deepening ( white arrows in Figure S5 ),  
752 corresponding to the difference between the filled square and filled circle.

753

754 For a variable  $Y$  whose vertical profile evolves with time while warming occurs simultaneously, the  
755 temporal change of  $Y$  on the density surface  $\sigma_A$  can be expressed as the sum of two components: the  
756 contribution due to the isopycnal deepening from  $z_A$  to  $z_B$  and the net temporal change of  $Y$ ,

757  $(\partial Y/\partial t)_{net}$  between the time before and after warming:

758 
$$\frac{\partial Y}{\partial t} = \left( \frac{\partial Y}{\partial z} \cdot \frac{\partial z}{\partial t} \right) + \left( \frac{\partial Y}{\partial t} \right)_{net} \quad (C4)$$

759 To evaluate the net change  $(\partial Y/\partial z)_{net}$  ( illustrated by the blue arrows of a difference in symbols  
760 between filled square and open square in Figure S5 ), it is necessary to evaluate the contribution of the  
761 temporal change of  $Y$  due to the isopycnal deepening and to subtract it from the change of  $Y$  observed  
762 at density  $\sigma_A$ . For instance, the change of  $O_2^{sat}$  in Figure S5 ( f ) is observed along the gray isopycnal  
763 surface ( large white arrow ), whereas the net change ( large blue and pink arrows ) is obtained as the  
764 difference between the observed change and the deepening effect.

765

766 The dissolved oxygen concentration  $O_2$  can be expressed as:

767 
$$O_2 = O_2^{sat} - AOU, \quad (C5)$$

768 where  $O_2^{sat}$  is the oxygen saturation concentration ( a function of temperature and salinity ), and AOU  
769 is “apparent oxygen utilization”, representing the oxygen consumed by biological processes since  
770 subduction. Near the surface, AOU is typically small, and its contributions can be neglected.

771

772 Following Eq. ( C4 ), the temporal change of  $O_2$  on a given isopycnal surface at a fixed station is:

773 
$$\frac{\partial O_2}{\partial t} = \left( \frac{\partial O_2}{\partial z} \cdot \frac{\partial z}{\partial t} \right) + \left( \frac{\partial O_2}{\partial t} \right)_{net}. \quad (C6)$$

774 Similarly,

775 
$$\frac{\partial O_2^{sat}}{\partial t} = \left( \frac{\partial O_2^{sat}}{\partial z} \cdot \frac{\partial z}{\partial t} \right) + \left( \frac{\partial O_2^{sat}}{\partial t} \right)_{net}, \quad (C7)$$

776 and

777 
$$\frac{\partial AOU}{\partial t} = \left( \frac{\partial(AOU)}{\partial z} \cdot \frac{\partial z}{\partial t} \right) + \left( \frac{\partial(AOU)}{\partial t} \right)_{net}. \quad (C8)$$

778 The term  $\text{net}$  is directly related to warming, because depends on temperature and salinity. If AOU does  
 779 not change with time, that is, if changes in  $O_2$  arise solely from changes in, then  $\partial(AOU)/\partial t$  follows  
 780 Eq. ( C3 ) and  $= 0$ . If AOU varies with time, however,  $\partial(AOU)/\partial t$  follows Eq. ( C4 ) and  $\neq 0$ , as  
 781 illustrated by the dashed gray line in Figure S5 ( g ).

782

783 Because  $O_2$  is defined by Eq. ( C5 ), the net temporal change of  $O_2$  on an isopycnal surface is

$$784 \quad \left(\frac{\partial O_2}{\partial t}\right)_{net} = \left(\frac{\partial O_2^{sat}}{\partial t}\right)_{net} - \left(\frac{\partial(AOU)}{\partial t}\right)_{net}. \quad (C9)$$

785 Combining Eqs. ( C6 ) and ( C9 ), the total temporal change of  $O_2$  on an isopycnal surface can be  
 786 written as

$$787 \quad \left(\frac{\partial O_2}{\partial t}\right) = \left(\frac{\partial O_2}{\partial z} \cdot \frac{\partial z}{\partial t}\right) + \left(\frac{\partial O_2^{sat}}{\partial t}\right)_{net} - \left(\frac{\partial(AOU)}{\partial t}\right)_{net}, \quad (C10)$$

788 which corresponds to Eq. ( 1 ) in the main text. Eq. ( C10 ) corresponds to an arrow in Figure S5 ( e ),  
 789 represented from left to right by the large gray arrow, white, blue, and pink arrows. The large blue  
 790 arrow is identical to Figure S5 ( f ), while the large pink arrow corresponds to Figure S5(g), but with  
 791 its direction reversed. Finally, substituting Eqs. ( C7 ) and ( C8 ) into ( C10 )

$$792 \quad \frac{\partial O_2}{\partial t} = \left(\frac{\partial O_2}{\partial z} \frac{\partial z}{\partial t}\right) + \left(\frac{\partial O_2^{sat}}{\partial t} - \frac{\partial O_2^{sat}}{\partial z} \frac{\partial z}{\partial t}\right) - \left(\frac{\partial(AOU)}{\partial t} - \frac{\partial(AOU)}{\partial z} \frac{\partial z}{\partial t}\right), \quad (C11)$$

$$793 \quad \text{( i) } \quad \text{( ii) } \quad \text{( iii) } \quad \text{( iv) } \quad \text{( v) } \quad \text{( vi)}$$

794 which corresponds to Eq. ( 2 ) in the main text. Note: The signs in terms ( v ) and ( vi ) in Eq. ( 3 ) are  
 795 reversed relative to those in Eq. ( C11 ) for convenience.

796

797 Table A1 The physical interpretation of each term in the oxygen tendency decomposition shown in Eq.  
 798 ( 3 ) and Eq. ( C11 ) is summarized.

Term	Mathematical form	Physical interpretation
(ii)	$(\partial O_2 / \partial z)(\partial z / \partial t)$	Vertical heave acting on the O <sub>2</sub> gradient
(iii)	$\partial O_2^{sat} / \partial t$	Solubility effect due to temperature and salinity changes
(iv)	$-(\partial O_2^{sat} / \partial z)(\partial z / \partial t)$	Vertical heave acting on the solubility gradient
(v)	$\partial AOU / \partial t$	AOU changes related to air–sea disequilibrium, biological activity and lateral circulation
(vi)	$-(\partial AOU / \partial z)(\partial z / \partial t)$	Vertical heave of the AOU gradient

799

800

801 **References:**

- 802 Alkire, M. B., D'Asaro, E., Lee, C., Jane Perry, M., Gray, A., Cetinić, I., et al. (2012). Estimates of  
803 net community production and export using high-resolution, Lagrangian measurements of O<sub>2</sub>, NO<sub>3</sub><sup>-</sup>,  
804 and POC through the evolution of a spring diatom bloom in the North Atlantic. *Deep Sea Research*  
805 *Part I: Oceanographic Research Papers*, 64, 157–174. <https://doi.org/10.1016/j.dsr.2012.01.012>
- 806 Behringer, D. W., & Xue, Y. (2004). Evaluation of the global ocean data assimilation system at NCEP:  
807 The Pacific Ocean. 8<sup>th</sup> Symposium on Integrated Observing and Assimilation Systems for Atmosphere,  
808 Oceans, and Land Surface, AMS 84<sup>th</sup> Annual Meeting, Washington State Convention and Trade Center,  
809 Seattle, Washington, 11-15. <https://ams.confex.com/ams/pdfpapers/70720.pdf>
- 810 Behringer, D. W. (2007). The Global Ocean Data Assimilation System (GODAS) at NCEP. 11th  
811 Symp. on Integrated Observing and Assimilation Systems for Atmosphere, Oceans, and Land  
812 Surface, San Antonio, TX, Amer. Meteor. Soc., 3.3. [Available online  
813 at <https://ams.confex.com/ams/pdfpapers/119541.pdf>.]
- 814 Berman-Frank, I., Lundgren, P., & Falkowski, P. (2003). Nitrogen fixation and photosynthetic oxygen  
815 evolution in cyanobacteria. *Research in Microbiology*, 154(3), 157–164.  
816 [https://doi.org/10.1016/S0923-2508\(03\)00029-9](https://doi.org/10.1016/S0923-2508(03)00029-9)

817 Bittig, H. C., Fiedler, B., Scholz, R., Krahnemann, G., & Körtzinger, A. (2014). Time response of oxygen  
818 optodes on profiling platforms and its dependence on flow speed and temperature. *Limnology and*  
819 *Oceanography: Methods*, 12(8), 617–636. <https://doi.org/10.4319/lom.2014.12.617>

820 Bittig, H. C., & Körtzinger, A. (2015). Tackling Oxygen Optode Drift: Near-Surface and In-Air  
821 Oxygen Optode Measurements on a Float Provide an Accurate in Situ Reference.  
822 <https://doi.org/10.1175/JTECH-D-14-00162.1>

823 Bittig, H. C., Körtzinger, A., Neill, C., van Ooijen, E., Plant, J. N., Hahn, J., et al. (2018a). Oxygen  
824 Optode Sensors: Principle, Characterization, Calibration, and Application in the Ocean. *Frontiers in*  
825 *Marine Science*, 4. <https://doi.org/10.3389/fmars.2017.00429>

826 Bittig, H. C., Steinhoff, T., Claustre, H., Fiedler, B., Williams, N. L., Sauzède, R., et al. (2018b). An  
827 Alternative to Static Climatologies: Robust Estimation of Open Ocean CO<sub>2</sub> Variables and Nutrient  
828 Concentrations From T, S, and O<sub>2</sub> Data Using Bayesian Neural Networks. *Frontiers in Marine Science*,  
829 5. <https://doi.org/10.3389/fmars.2018.00328>

830 Bopp, L., Resplandy, L., Orr, J. C., Doney, S. C., Dunne, J. P., Gehlen, M., et al. (2013). Multiple  
831 stressors of ocean ecosystems in the 21st century: projections with CMIP5 models. *Biogeosciences*,  
832 10(10), 6225–6245. <https://doi.org/10.5194/bg-10-6225-2013>

833 Boyer, T. P., and S. Levitus (1997), Objective Analyses of Temperature and Salinity for the World  
834 Ocean on a 1/48 Grid, vol. 11, NOAA Atlas NESDIS, Natl. Oceanic and Atmos. Admin., Silver Spring,  
835 Md.

836 Boyer, T. P., Antonov, J. I., Baranova, O. K., Coleman, C., Garcia, H. E., Grodsky, A., et al. (2013).  
837 World Ocean Database 2013. Retrieved from  
838 <https://repository.oceanbestpractices.org/handle/11329/357>

839 Breiman, L. (2001). Random Forests. *Machine Learning*, 45(1), 5–32.  
840 <https://doi.org/10.1023/A:1010933404324>

841 Breitburg, D., Levin, L. A., Oschlies, A., Grégoire, M., Chavez, F. P., Conley, D. J., et al. (2018).  
842 Declining oxygen in the global ocean and coastal waters. *Science*, 359(6371), eaam7240.  
843 <https://doi.org/10.1126/science.aam7240>

844 Bushinsky, S. M., Emerson, S. R., Riser, S. C., & Swift, D. D. (2016). Accurate oxygen measurements  
845 on modified Argo floats using in situ air calibrations. *Limnology and Oceanography: Methods*, 14(8),  
846 491–505. <https://doi.org/10.1002/lom3.10107>

847 Bushinsky, S.M., Nachod, Z., Fassbender, A.J., Tamsitt, V., Takeshita, Y., Williams, N., 2025. Offset  
848 Between Profiling Float and Shipboard Oxygen Observations at Depth Imparts Bias on Float pH and  
849 Derived pCO<sub>2</sub>. *Global Biogeochemical Cycles* 39, e2024GB008185.  
850 <https://doi.org/10.1029/2024GB008185>

851 Chen, X., Qiu, B., Du, Y., Chen, S., & Qi, Y. (2016). Interannual and interdecadal variability of the  
852 North Equatorial Countercurrent in the Western Pacific. *Journal of Geophysical Research: Oceans*,  
853 121(10), 7743–7758. <https://doi.org/10.1002/2016JC012190>

854 Claustre, H., Johnson, K. S., & Takeshita, Y. (2020). Observing the Global Ocean with  
855 Biogeochemical-Argo. *Annual Review of Marine Science*, 12(Volume 12, 2020), 23–48.  
856 <https://doi.org/10.1146/annurev-marine-010419-010956>

857 D’Asaro, E. A., & McNeil, C. (2013). Calibration and Stability of Oxygen Sensors on Autonomous  
858 Floats. <https://doi.org/10.1175/JTECH-D-12-00222.1>

859 Drucker, R., & Riser, S. C. (2016). In situ phase-domain calibration of oxygen Optodes on profiling  
860 floats. *Methods in Oceanography*, 17, 296–318. <https://doi.org/10.1016/j.mio.2016.09.007>

861 Estapa, M. L., Feen, M. L., & Breves, E. (2019). Direct Observations of Biological Carbon Export  
862 From Profiling Floats in the Subtropical North Atlantic. *Global Biogeochemical Cycles*, 33(3), 282–  
863 300. <https://doi.org/10.1029/2018GB006098>

864 Giglio, D., Lyubchich, V., & Mazloff, M. R. (2018). Estimating Oxygen in the Southern Ocean Using  
865 Argo Temperature and Salinity. *Journal of Geophysical Research: Oceans*, 123(6), 4280–4297.  
866 <https://doi.org/10.1029/2017JC013404>

867 Helm, K. P., Bindoff, N. L., & Church, J. A. (2011). Observed decreases in oxygen content of the  
868 global ocean. *Geophysical Research Letters*, 38(23). <https://doi.org/10.1029/2011GL049513>

869 Ito, T., Minobe, S., Long, M. C., & Deutsch, C. (2017). Upper ocean O<sub>2</sub> trends: 1958–2015.  
870 *Geophysical Research Letters*, 44(9), 4214–4223. <https://doi.org/10.1002/2017GL073613>

871 Ito, T., Cervania, A., Cross, K., Ainchwar, S., & Delawalla, S. (2024). Mapping Dissolved Oxygen  
872 Concentrations by Combining Shipboard and Argo Observations Using Machine Learning Algorithms.  
873 *Journal of Geophysical Research: Machine Learning and Computation*, 1(3), e2024JH000272.  
874 <https://doi.org/10.1029/2024JH000272>

875 Johnson, K. S., Plant, J. N., Riser, S. C., & Gilbert, D. (2015). Air Oxygen Calibration of Oxygen  
876 Optodes on a Profiling Float Array. <https://doi.org/10.1175/JTECH-D-15-0101.1>

877 Johnson, K. S., Plant, J. N., Coletti, L. J., Jannasch, H. W., Sakamoto, C. M., Riser, S. C., et al. (2017).  
878 Biogeochemical sensor performance in the SOCCOM profiling float array. *Journal of Geophysical*  
879 *Research: Oceans*, 122(8), 6416–6436. <https://doi.org/10.1002/2017JC012838>

880 Johnson, K. S., & Bif, M. B. (2021). Constraint on net primary productivity of the global ocean by  
881 Argo oxygen measurements. *Nature Geoscience*, 14(10), 769–774. [https://doi.org/10.1038/s41561-](https://doi.org/10.1038/s41561-021-00807-z)  
882 [021-00807-z](https://doi.org/10.1038/s41561-021-00807-z)

883 Kalnay, E., Kanamitsu, M., Kistler, R., Collins, W., Deaven, D., Gandin, L., et al. (1996). The  
884 NCEP/NCAR 40-Year Reanalysis Project. Retrieved from  
885 [https://journals.ametsoc.org/view/journals/bams/77/3/1520-](https://journals.ametsoc.org/view/journals/bams/77/3/1520-0477_1996_077_0437_tnyrp_2_0_co_2.xml)  
886 [0477\\_1996\\_077\\_0437\\_tnyrp\\_2\\_0\\_co\\_2.xml](https://journals.ametsoc.org/view/journals/bams/77/3/1520-0477_1996_077_0437_tnyrp_2_0_co_2.xml)

887 Kara, A. B., Rochford, P. A., & Hurlburt, H. E. (2000). An optimal definition for ocean mixed layer  
888 depth. *Journal of Geophysical Research: Oceans*, *105*(C7), 16803–16821.  
889 <https://doi.org/10.1029/2000JC900072>

890 Keeling, R. F., Körtzinger, A., & Gruber, N. (2010). Ocean Deoxygenation in a Warming World.  
891 *Annual Review of Marine Science*, *2* (Volume 2, 2010), 199–229.  
892 <https://doi.org/10.1146/annurev.marine.010908.163855>

893 Kolodziejczyk, N., Portela, E., Thierry, V., & Prigent, A. (2024). ISASO2: recent trends and regional  
894 patterns of ocean dissolved oxygen change. *Earth System Science Data*, *16*(11), 5191–5206.  
895 <https://doi.org/10.5194/essd-16-5191-2024>

896 Körtzinger, A., Schimanski, J., & Send, U. (2005). High Quality Oxygen Measurements from Profiling  
897 Floats: A Promising New Technique. <https://doi.org/10.1175/JTECH1701.1>

898 Kwiatkowski, L., Torres, O., Bopp, L., Aumont, O., Chamberlain, M., Christian, J. R., et al. (2020).  
899 Twenty-first century ocean warming, acidification, deoxygenation, and upper-ocean nutrient and  
900 primary production decline from CMIP6 model projections. *Biogeosciences*, *17*(13), 3439–3470.  
901 <https://doi.org/10.5194/bg-17-3439-2020>

902 Lauvset, S. K., Lange, N., Tanhua, T., Bittig, H. C., Olsen, A., Kozyr, A., et al. (2022b).  
903 GLODAPv2.2022: the latest version of the global interior ocean biogeochemical data product. *Earth*  
904 *System Science Data*, *14*(12), 5543–5572. <https://doi.org/10.5194/essd-14-5543-2022>

905 Li, C., Huang, Jianping, Ding, L., Liu, X., Yu, H., Huang, Jiping, 2020. Increasing Escape of Oxygen  
906 From Oceans Under Climate Change. *Geophysical Research Letters* *47*, e2019GL086345.  
907 <https://doi.org/10.1029/2019GL086345>

908 Limburg, K. E., Breitburg, D., Swaney, D. P., & Jacinto, G. (2020). Ocean Deoxygenation: A Primer.  
909 *One Earth*, *2*(1), 24–29. <https://doi.org/10.1016/j.oneear.2020.01.001>

910 Masumoto, Y., Sasaki, H., Kagimoto, T., Komori, N., Ishida, A., Sasai, Y., et al. (2004). A fifty-year  
911 eddy-resolving simulation of the world ocean: Preliminary outcomes of OFES (OGCM for the Earth

912 Simulator). *Journal of the Earth Simulator*, 1,35–56. [https://www.jamstec.](https://www.jamstec.go.jp/ceist/j/publication/journal/jes_vol.1/pdf/JES1-3.2-masumoto.pdf)  
913 [go.jp/ceist/j/publication/journal/jes\\_vol.1/pdf/JES1-3.2-masumoto.pdf](https://www.jamstec.go.jp/ceist/j/publication/journal/jes_vol.1/pdf/JES1-3.2-masumoto.pdf)

914 Masumoto, Y. (2010). Sharing the results of a high-resolution ocean general circulation model under  
915 a multi-discipline framework—a review of OFES activities. *Ocean Dynamics*, 60(3), 633–652.  
916 <https://doi.org/10.1007/s10236-010-0297-z>

917 Maurer, T. L., Plant, J. N., & Johnson, K. S. (2021). Delayed-Mode Quality Control of Oxygen, Nitrate,  
918 and pH Data on SOCCOM Biogeochemical Profiling Floats. *Frontiers in Marine Science*, 8.  
919 <https://doi.org/10.3389/fmars.2021.683207>

920 Nakamura, T., & Awaji, T. (2004). Tidally induced diapycnal mixing in the Kuril Straits and its role  
921 in water transformation and transport: A three-dimensional nonhydrostatic model experiment. *Journal*  
922 *of Geophysical Research: Oceans*, 109(C9). <https://doi.org/10.1029/2003JC001850>

923 Nakamura, T., Awaji, T., Hatayama, T., Akitomo, K., Takizawa, T., Kono, T., et al. (2000a). The  
924 Generation of Large-Amplitude Unsteady Lee Waves by Subinertial K1 Tidal Flow: A Possible  
925 Vertical Mixing Mechanism in the Kuril Straits. Retrieved from  
926 [https://journals.ametsoc.org/view/journals/phoc/30/7/1520-](https://journals.ametsoc.org/view/journals/phoc/30/7/1520-0485_2000_030_1601_tgolau_2.0.co_2.xml)  
927 [0485\\_2000\\_030\\_1601\\_tgolau\\_2.0.co\\_2.xml](https://journals.ametsoc.org/view/journals/phoc/30/7/1520-0485_2000_030_1601_tgolau_2.0.co_2.xml)

928 Nakamura, T., Awaji, T., Hatayama, T., Akitomo, K., & Takizawa, T. (2000b). Tidal Exchange  
929 through the Kuril Straits. Retrieved from [https://journals.ametsoc.org/view/journals/phoc/30/7/1520-](https://journals.ametsoc.org/view/journals/phoc/30/7/1520-0485_2000_030_1622_tetts_2.0.co_2.xml)  
930 [0485\\_2000\\_030\\_1622\\_tetts\\_2.0.co\\_2.xml](https://journals.ametsoc.org/view/journals/phoc/30/7/1520-0485_2000_030_1622_tetts_2.0.co_2.xml)

931 Nicholson, D. P., & Feen, M. L. (2017). Air calibration of an oxygen optode on an underwater glider.  
932 *Limnology and Oceanography: Methods*, 15(5), 495–502. <https://doi.org/10.1002/lom3.10177>

933 Ogata, T., & Nonaka, M. (2020). Mechanisms of Long-Term Variability and Recent Trend of Salinity  
934 Along 137°E. *Journal of Geophysical Research: Oceans*, 125(2), e2019JC015290.  
935 <https://doi.org/10.1029/2019JC015290>

936 Pacanowski, R. C., and S. M. Griffies (2000), MOM 3.0 Manual, Technical Report 4, 680 pp., Geophys.  
937 Fluid Dyn. Lab., Princeton, N. J. Philander, S. G. H. (1990), El Niño, La Niña, and the Southern  
938 Oscillation, pp. 293, Academic Press, San Diego, Calif.

939 Pörtner, H. O., & Farrell, A. P. (2008). Physiology and Climate Change. *Science*, 322(5902), 690–692.  
940 <https://doi.org/10.1126/science.1163156>

941 Pozo Buil, M., & Di Lorenzo, E. (2017). Decadal dynamics and predictability of oxygen and  
942 subsurface tracers in the California Current System. *Geophysical Research Letters*, 44(9), 4204–4213.  
943 <https://doi.org/10.1002/2017GL072931>

944 Reid, J. L. (1997). On the total geostrophic circulation of the pacific ocean: flow patterns, tracers, and  
945 transports. *Progress in Oceanography*, 39(4), 263–352. [https://doi.org/10.1016/S0079-](https://doi.org/10.1016/S0079-6611(97)00012-8)  
946 [6611\(97\)00012-8](https://doi.org/10.1016/S0079-6611(97)00012-8)

947 Roemmich, D., & Gilson, J. (2009). The 2004–2008 mean and annual cycle of temperature, salinity,  
948 and steric height in the global ocean from the Argo Program. *Progress in Oceanography*, 82(2), 81–  
949 100. <https://doi.org/10.1016/j.pocean.2009.03.004>

950 Sampaio, E., Santos, C., Rosa, I. C., Ferreira, V., Pörtner, H.-O., Duarte, C. M., et al. (2021). Impacts  
951 of hypoxic events surpass those of future ocean warming and acidification. *Nature Ecology &*  
952 *Evolution*, 5(3), 311–321. <https://doi.org/10.1038/s41559-020-01370-3>

953 Sasaki, H., Nonaka, M., Masumoto, Y., Sasai, Y., Uehara, H., & Sakuma, H. (2008). An Eddy-  
954 Resolving Hindcast Simulation of the Quasiglobal Ocean from 1950 to 2003 on the Earth Simulator.  
955 In K. Hamilton & W. Ohfuchi (Eds.), *High Resolution Numerical Modelling of the Atmosphere and*  
956 *Ocean* (pp. 157–185). New York, NY: Springer. [https://doi.org/10.1007/978-0-387-49791-4\\_10](https://doi.org/10.1007/978-0-387-49791-4_10)

957 Sasano, D., Takatani, Y., Kosugi, N., Nakano, T., Midorikawa, T., & Ishii, M. (2015). Multidecadal  
958 trends of oxygen and their controlling factors in the western North Pacific. *Global Biogeochemical*  
959 *Cycles*, 29(7), 935–956. <https://doi.org/10.1002/2014GB005065>

960 Sasano, D., Takatani, Y., Kosugi, N., Nakano, T., Midorikawa, T., & Ishii, M. (2018). Decline and  
961 Bidecadal Oscillations of Dissolved Oxygen in the Oyashio Region and Their Propagation to the  
962 Western North Pacific. *Global Biogeochemical Cycles*, 32(6), 909–931.  
963 <https://doi.org/10.1029/2017GB005876>

964 Schmidtko, S., Stramma, L., & Visbeck, M. (2017). Decline in global oceanic oxygen content during  
965 the past five decades. *Nature*, 542(7641), 335–339. <https://doi.org/10.1038/nature21399>

966 Sharp, J. D., Fassbender, A. J., Carter, B. R., Johnson, G. C., Schultz, C., Dunne, J. P. (2022). GOBAI-  
967 O<sub>2</sub>: A Global Gridded Monthly Dataset of Ocean Interior Dissolved Oxygen Concentrations Based on  
968 Shipboard and Autonomous Observations (NCEI Accession 0259304). NOAA National Centers for  
969 Environmental Information. Dataset. <https://doi.org/10.25921/z72m-yz67>.

970 Sharp, J. D., Fassbender, A. J., Carter, B. R., Johnson, G. C., Schultz, C., & Dunne, J. P. (2023).  
971 GOBAI-O<sub>2</sub>: temporally and spatially resolved fields of ocean interior dissolved oxygen over nearly 2  
972 decades. *Earth System Science Data*, 15(10), 4481–4518. <https://doi.org/10.5194/essd-15-4481-2023>

973 Stramma, L., Johnson, G. C., Sprintall, J., & Mohrholz, V. (2008). Expanding Oxygen-Minimum  
974 Zones in the Tropical Oceans. *Science*, 320(5876), 655–658. <https://doi.org/10.1126/science.1153847>

975 Stramma, L., Schmidtko, S., Bograd, S. J., Ono, T., Ross, T., Sasano, D., & Whitney, F. A. (2020).  
976 Trends and decadal oscillations of oxygen and nutrients at 50 to 300&thinsp;m depth in the equatorial  
977 and North Pacific. *Biogeosciences*, 17(3), 813–831. <https://doi.org/10.5194/bg-17-813-2020>

978 Stramma, L., & Schmidtko, S. (2021). Tropical deoxygenation sites revisited to investigate oxygen  
979 and nutrient trends. *Ocean Science*, 17(3), 833–847. <https://doi.org/10.5194/os-17-833-2021>

980 Suga, T., Takei, Y., & Hanawa, K. (1997). Thermostad Distribution in the North Pacific Subtropical  
981 Gyre: The Central Mode Water and the Subtropical Mode Water. Retrieved from  
982 [https://journals.ametsoc.org/view/journals/phoc/27/1/1520-](https://journals.ametsoc.org/view/journals/phoc/27/1/1520-0485_1997_027_0140_tditnp_2.0.co_2.xml)  
983 [0485\\_1997\\_027\\_0140\\_tditnp\\_2.0.co\\_2.xml](https://journals.ametsoc.org/view/journals/phoc/27/1/1520-0485_1997_027_0140_tditnp_2.0.co_2.xml)

984 Suga, T., Motoki, K., Aoki, Y., & Macdonald, A. M. (2004). The North Pacific Climatology of Winter  
985 Mixed Layer and Mode Waters. Retrieved from  
986 [https://journals.ametsoc.org/view/journals/phoc/34/1/1520-  
987 0485\\_2004\\_034\\_0003\\_tnpcow\\_2.0.co\\_2.xml](https://journals.ametsoc.org/view/journals/phoc/34/1/1520-0485_2004_034_0003_tnpcow_2.0.co_2.xml)

988 Takatani, Y., Sasano, D., Nakano, T., Midorikawa, T., & Ishii, M. (2012). Decrease of dissolved  
989 oxygen after the mid-1980s in the western North Pacific subtropical gyre along the 137°E repeat  
990 section. *Global Biogeochemical Cycles*, 26(2). <https://doi.org/10.1029/2011GB004227>

991 Takeshita, Y., Martz, T. R., Johnson, K. S., Plant, J. N., Gilbert, D., Riser, S. C., et al. (2013). A  
992 climatology-based quality control procedure for profiling float oxygen data. *Journal of Geophysical  
993 Research: Oceans*, 118(10), 5640–5650. <https://doi.org/10.1002/jgrc.20399>

994 Udaya Bhaskar, T. V. S., Sarma, V. V. S. S., & Pavan Kumar, J. (2021). Potential Mechanisms  
995 Responsible for Spatial Variability in Intensity and Thickness of Oxygen Minimum Zone in the Bay  
996 of Bengal. *Journal of Geophysical Research: Biogeosciences*, 126(6), e2021JG006341.  
997 <https://doi.org/10.1029/2021JG006341>

998 Winkler, L. W. (1888). Die Bestimmung des im Wasser gelösten Sauerstoffes. *Berichte Der Deutschen  
999 Chemischen Gesellschaft*, 21(2), 2843–2854. <https://doi.org/10.1002/cber.188802102122>

1000 Wolf, M. K., Hamme, R. C., Gilbert, D., Yashayaev, I., & Thierry, V. (2018). Oxygen Saturation  
1001 Surrounding Deep Water Formation Events in the Labrador Sea From Argo-O<sub>2</sub> Data. *Global  
1002 Biogeochemical Cycles*, 32(4), 635–653. <https://doi.org/10.1002/2017GB005829>

1003 Xu, L., Wang, K., & Wu, B. (2022). Weakening and Poleward Shifting of the North Pacific Subtropical  
1004 Fronts from 1980 to 2018. *Journal of Physical Oceanography*, 52(3), 399-417.  
1005 <https://doi.org/https://doi.org/10.1175/JPO-D-21-0170.1>

1006 Yang, H., Lohmann, G., Krebs-Kanzow, U., Ionita, M., Shi, X., Sidorenko, D., et al. (2020). Poleward  
1007 Shift of the Major Ocean Gyres Detected in a Warming Climate. *Geophysical Research Letters*, 47(5),  
1008 e2019GL085868. <https://doi.org/10.1029/2019GL085868>

1009 Yasuda, I. (2004). North Pacific Intermediate Water: Progress in SAGE (SubArctic Gyre Experiment)  
1010 and Related Projects. *Journal of Oceanography*, 60(2), 385–395.  
1011 <https://doi.org/10.1023/B:JOCE.0000038344.25081.42>

1012 You, Y. (2003). The pathway and circulation of North Pacific Intermediate Water. *Geophysical*  
1013 *Research Letters*, 30(24). <https://doi.org/10.1029/2003GL018561>

1014

1015

1016